



## ISTITUTO NAZIONALE DI RICERCA METROLOGICA Repository Istituzionale

Magnetic clustering of Ni<sup>2+</sup> ions in metal-ceramic nanocomposites obtained from Ni-exchanged zeolite precursors

This is the author's accepted version of the contribution published as:

*Original*

Magnetic clustering of Ni<sup>2+</sup> ions in metal-ceramic nanocomposites obtained from Ni-exchanged zeolite precursors / Barrera, G.; Tiberto, P.; Esposito, S.; Marocco, A.; Bonelli, B.; Pansini, M.; Manzoli, M.; Allia, P.. - In: CERAMICS INTERNATIONAL. - ISSN 0272-8842. - 44:14(2018), pp. 17240-17250. [10.1016/j.ceramint.2018.06.182]

*Availability:*

This version is available at: 11696/65906 since: 2021-02-09T17:03:59Z

*Publisher:*

Elsevier

*Published*

DOI:10.1016/j.ceramint.2018.06.182

*Terms of use:*

This article is made available under terms and conditions as specified in the corresponding bibliographic description in the repository

*Publisher copyright*

(Article begins on next page)

Manuscript Number: CERI-D-18-04364R2

Title: Magnetic Clustering of Ni<sup>2+</sup> Ions in Metal-Ceramic Nanocomposites  
obtained from Ni-Exchanged Zeolite Precursors

Article Type: Full length article

Keywords: Nanocomposites; Magnetic properties.

Corresponding Author: Dr. Gabriele Barrera,

Corresponding Author's Institution: INRIM

First Author: Gabriele Barrera

Order of Authors: Gabriele Barrera; Paola Tiberto; Serena Esposito;  
Antonello Marocco; Barbara Bonelli; Michele Pansini; Maela Manzoli;  
Paolo Allia

**Abstract:** Metal-ceramic nanocomposites containing nominal 15% wt. Ni were produced by a smart, scalable process involving a suitable thermal treatment of Ni-exchanged zeolite precursors, and were investigated by dc magnetic techniques between 2 and 300 K. Two main magnetic phases were detected in all studied materials: globular magnetic nanoparticles with average diameters in the 10-20 nm range, and Ni<sup>2+</sup> ions embedded in the host ceramic matrix. The blocking temperature of NiO nanoparticles is well above room temperature. The magnetic signal from nanoparticles dominates at high temperature; however, a clear paramagnetic signal from Ni<sup>2+</sup> ions emerges when the temperature is decreased. The magnetic moment per Ni ion is in agreement with typical values found in Ni-containing zeolites. Magnetic susceptibility and FC/ZFC curves point to the existence of a weak interaction among Ni<sup>2+</sup> ions (Néel temperature  $T_N < 15$  K) which results in the formation of ferrimagnetic-like clusters below about 30 K. In each cluster, the individual magnetic moments respond in a collective way with blocking temperatures less than 5 K.



Strada delle Cacce 91 - I-10125 Torino, Italy  
Tel ++39 (11) 3919-1  
Fax ++39 (11) 3919-834

Dr. Gabriele Barrera

Tel ++39 (11) 3919-858  
Fax ++39 (11) 3919-834  
E-mail g.barrera@inrim.it

---

The Authors thank the referee for his/her gratifying comments and suggestions which have been duly addressed. A complete list of the referee's comments and the related actions follows:

1. The authors are asked to correct the typographical error and grammatical error in the manuscript.

**DONE. The manuscript is, to the Authors' knowledge, free from typos or grammar errors**

2. Although the magnetic signal from nanoparticles dominates at high temperature, a clear paramagnetic signal from Ni<sup>2+</sup> ions is observed when the temperature is decreased. The authors must be rewriting this line.

**DONE. This line has been rewritten in the Abstract**

3. Introduction Part: The authors can give small introduction in first four lines about the properties and applications of semiconductor materials followed by magnetic metal oxides. It can be very helpful for the readers and they can easily understand. The authors may refer the following articles for the above lines.

Ceramics International, 44 (2018) 13247-13252., Journal of Superconductivity and Novel Magnetism 28 (2015), 2755-2766., Advanced Science, Engineering and Medicine 7 (2015), 672-682., J. Alloys Compds. 723 (2017) 1155-1161., Journal of nanoscience and nanotechnology 15 (2015), 4358-4366., Journal of Superconductivity and Novel Magnetism 27 (2014), 2725-2733., Journal of nanoscience and nanotechnology 13 (2013), 2986-2992., Transactions of Nonferrous Metals Society of China 25 (2015), 3271-3278.

**DONE. The Introduction now contains some additional lines about the features and applications of magnetic oxide nanostructures with semiconducting properties as well as the use of off-equilibrium thermal treatments to produce magnetic nanophases; all suggested references have been added.**

4. These transitions would arise from antiferromagnetic nanocrystals with anisotropy axis having a substantial component parallel to the applied field; finally, the hypothesis is contradicted also by the presence of a downward curvature in the high-field  $M(H)$  curves at low temperatures. The authors may cite the following papers in the Magnetic studies.

Ceramics International, 44 (2018) 5751-5759., Journal of Superconductivity and Novel Magnetism 29 (2016), 2141-2149., Journal of nanoscience and nanotechnology 16 (2016), 5929-5943., Journal of Superconductivity and Novel Magnetism 30 (2017), 691-699., Journal of Nanoscience and Nanotechnology 16 (2016), 7325-7336., Journal of Nanoelectronics and Optoelectronics 12 (2017), 1326-1333., Ceramics International, 44 (2018) 14242-14250.

**DONE. Some lines about the effect of magnetic ion doping of nanoferrites have been included in Section 4.2; all suggested references have been added.**

Yours sincerely,

A handwritten signature in dark ink, reading "Gabriele Barrera". The script is cursive and fluid, with the first name and last name clearly distinguishable.

(Gabriele Barrera)

Torino, June 21, 2018

# Magnetic Clustering of Ni<sup>2+</sup> Ions in Metal-Ceramic Nanocomposites obtained from Ni-Exchanged Zeolite Precursors

G. Barrera<sup>a,\*</sup>, P. Tiberto<sup>a</sup>, S. Esposito<sup>b</sup>, A. Marocco<sup>b</sup>, B. Bonelli<sup>c</sup>, M. Pansini<sup>b</sup>, M. Manzoli<sup>d</sup>, P. Allia<sup>c</sup>

<sup>a</sup> Nanoscience and Materials, INRiM, Strada delle Cacce 91, 10135 Torino Italy  
<sup>b</sup> Department of Civil and Mechanical Engineering and INSTM Research Unit, Università degli Studi di Cassino e del Lazio Meridionale, via G. Di Biasio 43, 03043 Cassino, FR, Italy  
<sup>c</sup> Department of Applied Science and Technology, Politecnico di Torino, Corso Duca degli Abruzzi 24, 10129 Torino, Italy  
<sup>d</sup> Department of Drug Science and Technology, Università degli Studi di Torino, Via Pietro Giuria 9, Torino, Italy

\*Corresponding author at: INRiM Torino, Strada delle Cacce 91, I-10135 Torino, Italy. E-mail address: [g.barrera@inrim.it](mailto:g.barrera@inrim.it)

## Abstract

Metal-ceramic nanocomposites containing nominal 15% wt. Ni were produced by a smart, scalable process involving a suitable thermal treatment of Ni-exchanged zeolite precursors, and were investigated by dc magnetic techniques between 2 and 300 K. Two main magnetic phases were detected in all studied materials: globular magnetic nanoparticles with average diameters in the 10-20 nm range, and Ni<sup>2+</sup> ions embedded in the host ceramic matrix. The blocking temperature of Ni<sup>0</sup> nanoparticles is well above room temperature. The magnetic signal from nanoparticles dominates at high temperature; however, a clear paramagnetic signal from Ni<sup>2+</sup> ions emerges when the temperature is decreased. The magnetic moment per Ni ion is in agreement with typical values found in Ni-containing zeolites. Magnetic susceptibility and FC/ZFC curves point to the existence of a weak interaction among Ni<sup>2+</sup> ions (Néel temperature

$T_N < 15$  K) which results in the formation of ferrimagnetic-like clusters below about 30 K. In each cluster, the individual magnetic moments respond in a collective way with blocking temperatures less than 5 K.

## Keywords

**B** Nanocomposites; **C** Magnetic properties

### 1. Introduction

In the last decade, the scientific interest towards magnetic nanostructured / nanocomposite materials has steadily increased owing to their functional properties associated with widespread applications ranging from electronics [1], magneto-optics and photocatalysis [2–5] to supercapacitors [6,7], hyperthermia [8], drug delivery [9,10], water remediation [11], energy harvesting [12]. Oxides of transition metals / rare earths have received particular attention because of the concurrence of magnetic effects and semiconducting-like properties [3,12,13]

Magnetic metal-ceramic nanocomposites, consisting of a dispersion of  $\text{Fe}^0$ ,  $\text{Co}^0$ , or  $\text{Ni}^0$  nanoparticles into a prevalingly amorphous silica and alumina ceramic matrix, are an important sub-class of nanomaterials whose fields of application are typically associated with their porous structure, which makes them particularly suitable for use in environmental protection [14–22], catalysis [23–28] and biomedicine [29–33].

The metal-ceramic nanocomposites studied in this paper were obtained from zeolite precursors by means of a smart and scalable process. Such a patented process [34–36] is essentially based on two simple operations:

- 1)  $\text{Fe}^{2+}$ ,  $\text{Co}^{2+}$ , or  $\text{Ni}^{2+}$  exchange of commercial zeolites;
- 2) Thermal treatment under reducing atmosphere of Fe-, Co-, or Ni-exchanged zeolites at relatively moderate temperatures (500-850 °C).

Recently, preparation methods involving off-equilibrium thermal treatments have been successfully exploited to produce nanostructured magnetic materials of high prospective impact in applications ranging from optics to asepsis [13,37–39]

The thermal process used to produce the nanocomposites investigated in the present work turn out to be inexpensive on account of the low cost of the raw materials and of its intrinsic simplicity and exhibits large potential for practical applications. On this basis, a long-term study on the production of magnetic metal-ceramic nanocomposites and on their various applications was undertaken [40–42]. For instance, nanocomposites formed by a dispersion of  $\text{Fe}^0$  nanoparticles into a prevalingly amorphous silica and alumina ceramic matrix were produced and used in the *Escherichia Coli* DNA separation [40] and in pesticides removal from water by adsorption [41], obtaining very encouraging results. Preparation details, morphology and prospective applications of nanocomposites containing  $\text{Ni}^0$  nanoparticles have been discussed elsewhere [42]. In this case, different nanocomposites formed starting from Ni-exchanged zeolites A and X were fully characterized in order to determine the impact of the operative conditions on the application-oriented properties of the final products.

An important part of the characterization involves the magnetic behavior of such products. The effect of the precursor zeolite on the standard magnetic properties at

1 room-temperature (high-field magnetization  $M_s$ , coercivity  $H_c$ ) has been briefly  
2  
3 discussed [42]; however, the magnetic properties of these materials pose a challenge  
4  
5 because of their complex structure and morphology as deduced from dedicated  
6  
7 analysis. As a matter of fact, an accurate picture of the magnetism of multi-phase  
8  
9 materials can only be achieved by means of a detailed study of magnetization and  
10  
11 magnetic susceptibility as functions of temperature, systematically exploiting the  
12  
13 available knowledge of their structure, composition and morphology.  
14  
15  
16  
17  
18

19  
20 In this paper, we focus on four different ceramic nanocomposites, obtained under  
21  
22 identical thermal treatments starting from both zeolite A and zeolite X. Despite the  
23  
24 differences between precursor zeolites and heat treatments, the samples exhibit  
25  
26 remarkable similarities in their magnetic behavior and allow one to draw a full picture  
27  
28 of the magnetic phenomena in these nanomaterials over a wide temperature range.  
29  
30  
31  
32

33  
34 Moreover, the present study shows how to generally interpret the complex magnetic  
35  
36 behavior of a variety of nanocomposites containing transition metals, where the  
37  
38 entities responsible for magnetism may experience different environments, or  
39  
40 different ionization states, or different degrees of aggregation, typically resulting in a  
41  
42 variety of entangled magnetic phases.  
43  
44  
45  
46  
47  
48  
49  
50  
51  
52  
53  
54  
55  
56  
57  
58  
59  
60  
61  
62  
63  
64  
65



## 2. Material and Methods

### 2.1 Sample preparation and structural/morphological characterization

Full details of the preparation of metal-ceramic nanocomposites have been published elsewhere [42]. A short summary of the various steps in the preparation process follows:

#### a) preparation of $\text{Ni}^{2+}$ -exchanged zeolites

The parent A/X zeolites were contacted with a  $[\text{Ni}^{2+}] = 0.1 \text{ M}$  solution at a wt. solid/liquid ratio of  $(\text{S/L}) = 1/20$ , temperature  $(T) \approx 60 \text{ }^\circ\text{C}$ , and contact time  $(t) = 2 \text{ h}$ . The solid was separated from the liquid through filtration and contacted anew with a fresh solution; the procedure was iterated 10/6 times in A/X zeolite, respectively. The resulting powders, washed in distilled water, were dried for about one day at  $80 \text{ }^\circ\text{C}$ , and stored for at least 3 days in an environment with about 50% relative humidity to allow water saturation of zeolites. Cation-exchange operations are accurately described in refs. [43–45].

#### b) preparation of metal-ceramic nanocomposites

Two  $\text{Ni}^{2+}$ -exchanged zeolites A and X were submitted to thermal treatment under a reducing atmosphere under the following conditions:

1) Heating from room temperature up to  $735 \text{ }^\circ\text{C}$  ( $15 \text{ }^\circ\text{C}/\text{min}$  heating rate) and subsequent isothermal treatment for 12 min. The heating system of the furnace was then switched off and the sample was left to cool down to room temperature within

the furnace. These samples are referred to as NiA735C-12min and NiX735C-12min, respectively.

2) Heating from room temperature up to 750 °C (15 °C/min heating rate). As soon as the temperature of 750 °C was attained, the heating system of the furnace was switched off and the sample cooled down to room temperature within the furnace.

These samples are referred to as NiA750C-0min and NiX750C-0min.

Composition, structure and morphology of the four samples were studied by atomic absorption spectrophotometry, synchrotron radiation powder diffraction, X-ray powder diffraction, transmission electron microscopy (TEM) and high resolution TEM; the results have been published in Ref. [42].

## *2.2 Magnetic measurements*

Hysteresis loops were measured using a Quantum Design MPMS SQUID magnetometer (maximum field: 70 kOe) operating in the temperature range 2 K – 300 K. FC/ZFC curves were measured between 2 K and 300 K using the same magnetometer under an applied field of 50 Oe at a constant dT/dt rate of about 6 K/min.

### 3. Results

#### 3.1 Structure and morphology

A complete study of structure, composition and morphology of the present metal-ceramic nanocomposites is found in Ref. [42]; the interpretation of our magnetic results will be based upon the following facts:

- a) the weight percentage of Ni of the parent Ni-exchanged A and X zeolites is 15.0 and 14.4 %, respectively, as referred to dehydrated samples;
- b) the thermal treatment of the Ni-exchanged zeolites under reducing atmosphere results in different nanocomposite systems; the quantitative phase analysis (QPA) of powder diffraction patterns under synchrotron radiation is reported in Tab. 1 (taken from [42]) and indicates the presence of: 1) a residual fraction of untransformed zeolite in nanocomposites resulting from A zeolite (this fraction being almost negligible in nanocomposites resulting from X zeolite); 2) a considerable fraction of metallic Ni ( $\text{Ni}^0$ ) constituting the observed nanoparticle phase; 3) some Ni-oxide contribution (larger in nanocomposites resulting from X zeolite) and 4) some Nickel Hydride  $\text{HfNi}_2$  (in nanocomposites resulting from A zeolite only). All these phases are embedded in a dominant amorphous phase produced by collapse of  $\text{Ni}^{2+}$ -exchanged zeolites by effect of furnace treatments. A comparison of these results with the weight percentage of Ni of dehydrated Ni-exchanged A and X zeolites clearly indicates that a significant fraction of  $\text{Ni}^{2+}$  ions is still contained in the amorphous phase.

c) a selection of unpublished micrographs of samples NiA735C-12min (panel a), NiA750C-0min (panel b), and NiX735C-12min (panel a), NiX750C-0min (panel b) is reported in Figures 1-2, respectively. Nanocomposite materials obtained according to the above outlined procedure are made up by metal nanoparticles, with globular shape, in which Ni is in the cubic crystalline phase [42]. In all samples, the analysis of the TEM images shows that the average size of the Ni nanoparticles ranges between 13 and 18 nm [42]. In particular, the Ni<sup>0</sup> particle size distribution of NiA735C-12min (mean diameter=  $17.6 \pm 5.8$  nm) is slightly broader than the one obtained for NiA750C-0min (mean diameter=  $16.7 \pm 4.2$  nm). This is originated by the instantaneous drop of the temperature at 750 °C, favouring crystal nucleation rather than crystal growth. Independently of the thermal treatment conditions, homogeneously dispersed Ni nanoparticles embedded in hedgehog-like agglomerates were observed in NiX735C-12min (mean diameter=  $12.7 \pm 3.7$  nm) and NiX750C-0min (mean diameter=  $13.5 \pm 3.6$  nm) samples.

### *3.1 Magnetic properties*

The hysteresis loops  $M(H)$  of samples NiA735C-12min and NiX750C-0min are shown in Figure 3 after subtracting the weak diamagnetic signal from the nonmagnetic fraction of the nanocomposite and from the sample holder. The curves are representative of the  $M(H)$  behavior in all samples. The loops are generally characterized by a nonzero temperature-dependent coercive field  $H_c$  (see insets in Figure 3 for details of the hysteretic features of the curves) and by a non-saturating behavior at high fields, which becomes particularly evident below 100 K. The temperature dependence of the

coercive field is shown in Figure 4;  $H_c$  increases with decreasing temperature and is quite independent of the heat treatment during sample preparation. Nanocomposites resulting from A zeolite exhibit a slightly larger coercivity at all temperatures, in agreement with previous results [42]. The non-saturating behavior of the  $M(H)$  curves is mirrored by the behavior of the magnetization measured at  $H = 70$  kOe ( $M_{70\text{kOe}}$ ) as a function of temperature, as reported in Figure 5. All curves exhibit a marked upward bending as the temperature becomes lower than 100 K.

The FC-ZFC magnetization curves of all samples are shown in Figure 6. The FC and ZFC curves become separate exactly at room temperature, indicating that the blocking temperature of  $\text{Ni}^0$  nanoparticles is well above room temperature [46]. Both FC and ZFC curves are almost featureless over nearly all the examined temperature range (typically, above 30 K): FC curves are almost flat whereas the ZFC magnetization increases almost linearly with  $T$ . A low-temperature anomaly is observed for all nanocomposites; the details of the low- $T$  anomaly are put in evidence in Figure 7 for two representative samples: a monotonic increase of  $M_{500\text{e}}(T)$  and a bump of  $M_{500\text{e}}(T)$  appear to be superimposed to the featureless FC and ZFC curves, respectively. The effect can be singled out by extrapolating the FC/ZFC curves down to low temperature, as shown by the dashed lines in Figure 7, and by subtracting the baseline (corresponding to the low-temperature extrapolation of the featureless FC/ZFC curves) from the experimental data; the result is shown in Figure 8 for all nanocomposites. In samples NiA735C-12min, NiX735C-12min, NiA750C-0min (panels (a) to (c)) the subtracted FC and ZFC curves become separate immediately above a sharp maximum of the subtracted ZFC curve, which occurs between 4 and 5 K; in sample NiX750C-0min

(panel (d)) the data were taken starting from 5.5 K and the subtracted FC/ZFC curves appear to be still merged.

The non-saturating behavior of the magnetization of all nanocomposites has been studied by evaluating the differential dc susceptibility  $\chi_{\text{HF}}$  at high fields ( $H = 60$  kOe) for each experimental  $M(H)$  curve. The reciprocal of the susceptibility  $\chi_{\text{HF}}^{-1}$  is reported as a function of temperature in Figure 9.

## 4. Discussion

### 4.1 Contribution from Ni nanoparticles

Isothermal hysteresis loops (Figure 3) indicate that a substantial contribution from a non-saturating magnetic phase gradually emerges when the temperature is lowered, distinctly adding to a saturating contribution. Such an effect is observed in all samples and is reflected by the behavior of the  $M_{70\text{kOe}}(T)$  curves shown in Figure 5. It should be noted that the non-saturating contribution to  $M(H)$  is initially linear, but a downward curvature appears at sufficiently low temperatures.

The saturating contribution – predominant above 100 K - is attributed to Ni nanoparticles. Densely packed  $\text{Ni}^0$  nanoparticles have been put in evidence by TEM observations (Figures 1-2 and [42]). In the materials considered here, the content of Ni hydride ( $\text{H}\text{Ni}_2$ ) which contributes to the magnetic signal as well, is very small ( max 0.7 wt% [42]); moreover, it is known [47] that nickel hydride nanoparticles are

1 characterized by a ferromagnetic behaviour even at high H concentrations (up to  
2  
3  
4  $[H]/[Ni] = 1$ ), indicating that this contribution adds to the one from the dominant  $Ni^0$   
5  
6 phase.  
7

8  
9  
10 In spite of the lack of distinctive features in FC/ZFC curves over most of the explored  
11  
12 temperature range (the low-temperature anomaly will be considered in paragraph  
13  
14 4.5), there is a good general agreement between the nanoparticle size distribution  
15  
16 obtained from TEM and the one derived from the standard method of analysis  
17  
18 exploiting the difference between FC and ZFC curves [42].  
19  
20  
21  
22

#### 23 *4.2 Paramagnetic phase in metal-ceramic nanocomposites.*

24

25  
26  
27 Generally speaking, controlled introduction of specific magnetic ion species such as  
28  
29  $Mn^{2+}$ ,  $Ni^{2+}$  in magnetic/nonmagnetic hosts, such as doping of ferrite nanoparticles  
30  
31 [48,49] brings about interesting changes in their magnetic properties [50–54].  
32  
33  
34

35  
36 In the present case, the  $Ni^{2+}$  ions non concurring in the formation of zerovalent Ni  
37  
38 nanoparticles are dissolved in a non-magnetic host and are responsible for the non-  
39  
40 saturating magnetization observed at low temperatures which could originate from  
41  
42 either an antiferromagnetic phase with random anisotropy axes, or a paramagnetic  
43  
44 phase.  
45  
46  
47

48  
49 Although multi-phase magnetic nanosystems can exhibit specific antiferromagnetic  
50  
51 features [50], the hypothesis of an antiferromagnetic contribution in these zeolites is  
52  
53 contradicted by structural and magnetic results: X-ray diffraction rules out the  
54  
55 presence of a large fraction  $f_{NiO}$  of Ni oxides in nanocomposites resulting from A  
56  
57  
58  
59  
60  
61  
62  
63  
64  
65

zeolites ( $f_{\text{NiO}} \approx 1 \text{ wt\%}$ ); although a slightly larger fraction is found in materials deriving from X zeolites ( $f_{\text{NiO}} \approx 5 \text{ wt\%}$  [42]), this is not enough to explain the observed effect in terms of antiferromagnetism; moreover, the Ni oxide phase present in these nanocomposites has no definite stoichiometry and is expected to be in nanoparticle form; the ideal antiferromagnetic order typically disappears in Ni oxide nanoparticles giving rise to uncompensated magnetic moments [55]. In addition, no trace of metamagnetic transitions (such as spin flip or spin flop transitions [56]) are observed here. These transitions would arise from antiferromagnetic nanocrystals with anisotropy axis having a substantial component parallel to the applied field; finally, the hypothesis is contradicted also by the presence of a downward curvature in the high-field  $M(H)$  curves at low temperatures.



Indeed, such a curvature is typical of a paramagnetic response (corresponding to the non-linear behavior of the Brillouin function at sufficiently high fields and sufficiently low temperatures). Another fact pointing to a paramagnetic effect is the strong reduction of the non-saturating signal in the high temperature limit. The paramagnetic phase is therefore related to the presence of independent, bivalent Ni cations embedded in the ceramic matrix. Isolated  $\text{Ni}^{2+}$  ions are often found in Ni-exchanged zeolites [57–59]; their magnetic moments can take a variety of values, roughly ranging from 1.9 to 3.9 Bohr magnetons ( $\mu_B$ ) in dependence of the degree of quenching of the orbital momentum - which crucially depends in turn on the nature and symmetry of the immediate surroundings of the cations [60–64]. Indeed, both nature and symmetry of the environment vary in dependence of the actual localization on  $\text{Ni}^{2+}$  ions within the zeolite structure ( $\text{Ni}^{2+}$  sites can be found either in the supercage or sodalite cavities, or in exagonal cavities, or inside particles or clusters of NiO) [59].

The existence of a paramagnetic phase is strongly supported by the  $\chi_{\text{HF}}^{-1}$  vs. T curves reported in Figure 9<sup>A</sup>. These curves exhibit common features, namely: high-temperature data ( $T \geq 200$  K) lie on a straight line intersecting the horizontal axis at small, negative values (red lines in Figure 9); at intermediate temperatures ( $50 \text{ K} < T < 200 \text{ K}$ ) the experimental curves deviate from the linear behavior, showing a downward

---

<sup>A</sup> As a matter of fact, the standard analysis of a material's paramagnetic response makes use of the initial susceptibility  $\chi_0 = \lim_{H \rightarrow 0} \frac{dM}{dH}$  instead of the quantity  $\chi_{\text{HF}} = \left( \frac{dM}{dH} \right)_{H=60 \text{ kOe}}$ . However, the latter parameter was preferred because of the masking effect of the Ni-nanoparticle contribution, which dominates at low fields.

concavity; at even lower temperatures a broad minimum is observed. Such deviations from the linear behavior indicate that a weak interaction exists among paramagnetic units in our samples. From the linear fit it is possible to extract the Curie constant and the Néel temperature for all samples; these are reported in Table I. The downward concavity of the  $\chi_{\text{HF}}^{-1}$  vs. T curves at intermediate temperatures indicates that the interaction among paramagnetic units is basically ferrimagnetic; this can be put in evidence by plotting the product  $\chi_{\text{HF}}T$  as a function of temperature [65–68], as done in Figure 10 (symbols). The onset of a ferrimagnetic ordering is marked by the appearance of a shallow minimum in the  $\chi_{\text{HF}}T$  curve, followed by an increase at lower temperatures [66–68]. The drop of  $\chi_{\text{HF}}T$  below 50 K will be discussed later.

The effective magnetic moment per paramagnetic unit is obtained from the

experimental Curie constant using the standard expression  $\mu_{\text{eff}} = \left[ \frac{3k_B C}{Nf} \right]^{\frac{1}{2}}$ . The

number of paramagnetic units per gram is  $N \times f$ ,  $N$  being the total number of Ni atoms/ions per unit mass in our nanocomposites; starting from the  $\text{Ni}^{2+}$  meq/g values reported in Ref. [42], one gets  $N = 1.238 \times 10^{21}$  at/g and  $N = 1.123 \times 10^{21}$  at/g in nanocomposites resulting from A/X zeolite, respectively. The paramagnetic fraction  $f$  is easily obtained from the QPA data of Ref. [42] and is reported in Table I. The resulting effective number of Bohr magnetons per paramagnetic ion  $n_{\text{eff}}$  is reported in Table I also. The quantity  $\mu_{\text{eff}} = n_{\text{eff}} \mu_B$  turns out to be compatible with the magnetic moments on  $\text{Ni}^{2+}$  ions dispersed in zeolites available in the literature [60–64] and indicates that the paramagnetic units in our nanocomposites are single bivalent Ni ions (at high

temperatures at least). In nanocomposites resulting from zeolite A, the effective magnetic moment is lower and closer to the ideal value for isolated Ni ions with almost complete quenching of the orbital angular momentum.

An estimate of the saturation magnetization of Ni nanoparticles can be obtained considering that the sample magnetization measured at high-fields and at high temperature,  $M_{exp}$  can be approximately written as:

$$M_{exp} \cong Nf \frac{\mu_{eff}^2 H_{Max}}{3k_B T_{Max}} + M_{NP}^* (1 - f) \quad (1)$$

where  $H_{Max} = 70$  kOe,  $T_{Max} = 300$  K. In Eq. (1) the total magnetization is thought to be the sum of the contribution from paramagnetic Ni ions (whose response at 300 K is basically still linear even under fields as large as  $H_0$ ) and the contribution from magnetic nanoparticles, which is presumed to be fully saturated at  $H = H_0$ . The only unknown parameter in Eq. (1) is the intrinsic magnetization of Ni nanoparticles  $M_{NP}^*$ ; using the results for  $\mu_{eff}$ , one gets for  $M_{NP}^*$  the values shown in Table I. These are remarkably similar to each other and in very good agreement with the data available in the literature ( $\approx 35$  emu/g [69]) for a mean NP diameter comparable to the one observed in these materials, i.e., ranging between 12.7 nm (our sample NiX735C-12min) and 17.6 (our sample NiA735C-12min) [42].

#### 4.3 Magnetic clusters of $Ni^{2+}$ ions at low temperature

The low-temperature structure observed in the FC/ZFC curves (Figures 7 and 8) indicates some blocking effect at temperatures  $T_B$  of the order of 3-4.5 K; in sample

NiX750C-0min the absence of low-temperature measurements prevents  $T_B$  to be observed. As previously stated, the magnetic nanostructures which undergo this blocking cannot be the  $Ni^0$  nanoparticles. As a consequence, we infer that at low temperatures the interaction among individual  $Ni^{2+}$  ions put in evidence by the  $T\chi_T$  curves (Figure 10) results in the formation of ferrimagnetic-like clusters of interacting  $Ni^{2+}$  ions; the magnetic moments in each cluster are thought to be collectively responding to the magnetic field. The distribution  $p(T_B)$  of  $T_B$  values is quite narrow although not delta-like, as put in evidence by applying the standard analysis involving the derivative of the difference between ZFC and FC curves [70,71]. An example of the  $p(T_B)$  distribution estimated in this way is shown in Figure 11 for sample NiA750-0min. The mean blocking temperature of clusters  $\langle T_B \rangle$  is reported in Table II along with the mean barrier height expressed in Kelvin,  $U/k_B$ , obtained from the usual expression  $U/k_B = \ln(\tau_{exp}/\tau_0) \langle T_B \rangle$  taking  $\tau_{exp} = 100$  s and  $\tau_0 = 1 \times 10^{-7}$  s or  $\tau_0 = 1 \times 10^{-9}$  s (the first value being appropriate to single molecule magnets and small clusters [72], the second one being the usually accepted value for magnetic nanoparticles [73]).

These barrier heights have values comparable to the ones observed in many single-molecule magnets [72], and confirm that the clusters formed by interacting  $Ni^{2+}$  ions are very small. The presence of a large magnetic contribution from  $Ni^0$  nanoparticles prevents typical quantum effects related to the response of magnetic clusters or molecules, such as quantum tunneling of magnetization and definite hysteresis-loop steps [72] to be observed in the present case.

#### 4.4 Magnetic moment of low-temperature clusters

An estimate of the net magnetic moment of Ni<sup>2+</sup>-rich clusters can be obtained from a study of the high-field magnetization as a function of temperature. The experimental M<sub>70kOe</sub> (T) curve of Figure 5 is written as the sum of two contributions, from Ni<sup>0</sup> nanoparticles and from Ni<sup>2+</sup> ions respectively, the latter term being in principle proportional to a Brillouin function:

$$M_{70kOe}(T) = (1 - f)M_{NP}(T) + Nf\mu_0 B_J(x)$$
$$\mu_0 = g_J J \mu_B$$
$$x = x(T) = \frac{g_J \mu_B J H}{k_B T} \Big|_{H=70 \text{ kOe}} \quad (2)$$

In this expression M<sub>NP</sub>(T) is the saturation magnetization of the Ni nanoparticles (magnetic moment per gram of material) which is directly related to the intrinsic magnetization M\*<sub>NP</sub> by the relation M<sub>NP</sub> = αM\*<sub>NP</sub> with α = 0.15 or 0.144 in nanocomposites resulting from A/X zeolites, respectively. The temperature dependence of M<sub>NP</sub>(T) is taken equal to the one of bulk crystalline Ni [74]; the assumption is justified by the large size of our Ni nanoparticles and from the features of the FC/ZFC curves. The available literature confirms this assumption [75].

The n<sub>eff</sub> values of Table I indicate incomplete orbital quenching (J = 1, g<sub>J</sub> = 2 for complete quenching ; J = 4, g<sub>J</sub> = 5/4 for no quenching). In fact, all M<sub>70kOe</sub> (T) curves of Figure 5 can be accurately fitted at high temperatures by using either the B<sub>J=1</sub>(x) or the

$B_{J=4}(x)$  function, which are almost completely overlapping there; however, both curves fail to fit the low-temperature region of the experimental curve (below about 80 K). A typical example is shown in Figure 12 for sample NiX735C-12min; this behavior is representative of all investigated samples. On the contrary, the low-temperature region of the  $M_{70kOe}(T)$  curve is well fitted by the following expression:

$$\begin{aligned}
 M_{70kOe}(T) &= (1 - f)M_{NP}(T) + Nf\mu_{clust}L(x) \\
 x &= \left. \frac{\mu_{clust}H}{k_B T} \right|_{H=70 \text{ kOe}}
 \end{aligned} \tag{3}$$

where  $L(x)$  is the Langevin function (blue line in Figure 12). The effective magnetic moments emerging from the low-temperature fit ( $\mu_{clust}$ ) turns out to be considerably larger than the  $\mu_{eff}$  values obtained at high temperature, as shown in Table I. This result (which supports the choice of using a Langevin function instead of a Brillouin function in Eq.(3) ) is in good agreement with our interpretation of low-temperature data in terms of magnetic clusters rather than from isolated magnetic ions. In the intermediate region ( $30 \text{ K} \leq T \leq 70 \text{ K}$ ) neither Eq. (3) nor Eq. (2) correctly fit the experimental data, indicating a broad transition between the single-ion and the cluster regimes.

In the studied nanocomposites, the average magnetic moment of a cluster turns out to be of the order of 9.2 and  $10.5 \mu_B$  for materials obtained starting from A/X zeolites,

respectively (Table I). Both values are compatible with the presence of magnetic clusters carrying a net magnetic moment. Indeed, first-principles calculations indicate that clusters or ultra-small particles of Nickel compounds may exhibit a net magnetic moment of the order of a few Bohr magnetons originating from either imperfect pairing of antiparallel moments or competition between ferromagnetic and antiferromagnetic exchange integrals [61,76,77].

The present results provide an independent evidence of the appearance of magnetic clusters made of correlated ionic moments; the net magnetic moments associated to each cluster can be viewed as individually responding to the magnetic field and undergo blocking at the temperatures derived from the ZFC/FC curve analysis of the previous section.

The ferrimagnetic features put in evidence by the  $\chi_{\text{HF}}^{-1}$  (T) curve and by the behavior of the product  $\chi_{\text{HF}}T$  (Figures 9 and 10) suggest that an imperfect antiferromagnetic order exists among the individual ionic moments contained in each cluster; as a result, clusters exhibit the net magnetic moments shown in Table I. Remarkably, this view is supported by the behavior of the  $\chi_{\text{HF}}T$  data at low temperature. The blue curves of Figure 10 are generated by assuming that the magnetic moments are non-interacting and take the value  $\mu_{\text{clust}}$  instead of  $\mu_{\text{eff}}$ ; these curves fit very well the experimental  $\chi_{\text{HF}}T$  data in the low-temperature region (up to about 40 K), supporting the picture of interacting single-ion moments forming magnetic clusters at low T. On the contrary, the red curves, generated using  $\mu_{\text{eff}} = n_{\text{eff}}\mu_{\text{B}}$  under the assumption of non-interacting moments, fit the same data at high temperatures; the slight discrepancy between

experimental data and red curves indicates that single-ion moments are ferrimagnetically interacting. A transition region between the two regimes is observed.

#### *4.5 Range of existence of low-temperature clusters*

Analysis of the FC/ZFC curves (Figure 8) and fits of the  $M_{70\text{K Oe}}(T)$  curves (Figure 12) consistently indicate that magnetic clusters are stable at very low temperatures but gradually lose their identity above 30 K. The temperature where the ferrimagnetic-like clusters vanish can be viewed as a sort of Curie temperature ( $T_{\text{C clust}} \cong 30$  K); such a temperature is larger than the (absolute value of) the Néel temperature (Table I). Now, in macroscopic ferrimagnets containing two magnetic sublattices (A e B),  $T_{\text{C}}$  and  $T_{\text{N}}$  are given by different expressions containing many compositional and physical parameters [78,79] and are in general different from each other; when the A and B sublattices have similar numbers of ions per unit volume it is often found that  $T_{\text{C}} \cong T_{\text{N}}$  [78,79]. However, the result  $T_{\text{C}} > T_{\text{N}}$  is easily obtained when the balance between numbers of A and B ions is uneven [78]. In the present case the macroscopic formulas based upon the assumption of perfect, infinite magnetic sublattices clearly do not apply; the present results ( $T_{\text{C clust}} \cong 30$  K, whereas  $T_{\text{N}} \cong 3\text{-}13$  K) may be related to an imbalance between the numbers of up and down magnetic moments in each cluster.

## **5. Conclusion**



1 Thermal treatment under reducing atmosphere of Ni<sup>2+</sup>-substituted zeolites A and X  
2  
3 produces ceramic nanocomposites made up by zerovalent Ni nanoparticles embedded  
4  
5 in an amorphous ceramic phase resulting from decomposition of the zeolitic  
6  
7 precursors. The nanoparticles keep their morphological identity and give the  
8  
9 quantitatively dominant contribution to the magnetic signal at all temperatures.  
10  
11 However, the process leading to nanoparticle formation is incomplete, and a  
12  
13 substantial fraction of Ni<sup>2+</sup> cations appears to be sparsely trapped in the amorphous  
14  
15 ceramic phase.  
16  
17  
18  
19  
20  
21

22 A combined study of FC/ZFC curves, isothermal M(H) loops and high-field susceptibility  
23  
24 vs. temperature curves supported by morphologic and structural data makes it  
25  
26 possible to disentangle the contributions from the various magnetic phases, allowing a  
27  
28 detailed picture of the magnetic system to be drawn. In particular, the disperse Ni<sup>2+</sup>  
29  
30 cations give a paramagnetic response at high temperature, the magnetic moment per  
31  
32 ion being found to be comparable to the values typically observed in similar systems.  
33  
34 However, the presence of interactions among ionic moments results in the appearance  
35  
36 at low temperature of ferrimagnetic-like clusters which group a small number of  
37  
38 nearby ionic moments. Our measurements indicate that the clusters bear a net  
39  
40 magnetic moment of about 10 Bohr magnetons, i.e., about 5 times larger than the  
41  
42 moment on a single Ni ion; however, the number of ions involved in each cluster can  
43  
44 be larger than 5 because of the ferrimagnetic nature of the spin arrangement. The  
45  
46 clusters undergo individual blocking at very low temperatures (< 5 K); the  
47  
48 corresponding barrier energy is of the same order of magnitude of similar quantities  
49  
50  
51  
52  
53  
54  
55  
56  
57  
58  
59  
60  
61  
62  
63  
64  
65

1 obtained in some molecular magnets, again confirming that these clusters involve a  
2  
3  
4 small number of magnetic ions.  
5  
6

7 The following overall picture of the magnetic regimes in these ceramic  
8  
9 nanocomposites emerges: the magnetic signal from the nanoparticle phase mostly  
10  
11 comprised of  $\text{Ni}^0$  and – to a much lesser extent -  $\text{HfNi}_2$  nanoparticles is characterized by  
12  
13 featureless FC/ZFC curves and by saturating isothermal magnetization loops, whereas  
14  
15 the fraction of dispersed  $\text{Ni}^{2+}$  ions exhibits a more complex, temperature-dependent  
16  
17 behavior: at sufficiently high temperature the units responding to the magnetic field  
18  
19 are the individual, disperse  $\text{Ni}^{2+}$  ions; the weak interaction among ions leads to the  
20  
21 onset of a ferrimagnetic order and to the appearance of clusters characterized by a net  
22  
23 magnetic moment. Below the ordering temperature, the magnetic units individually  
24  
25 responding to the applied field are these clusters and not the single  $\text{Ni}^{2+}$  ions; the  
26  
27 cluster magnetic moments become blocked at a very low temperature.  
28  
29  
30  
31  
32  
33  
34  
35

## 36 **Funding**

37  
38  
39

40 This research did not receive any specific grant from funding agencies in the public,  
41  
42 commercial, or not-for-profit sectors.  
43  
44  
45

## 46 **Declaration of interest**

47  
48

49 Declarations of interest: none.  
50  
51  
52  
53  
54  
55  
56  
57  
58  
59  
60  
61  
62  
63  
64  
65

## References

- [1] L. Jun, X. Guozhi, J. Peicheng, Q. Jie, C. Jiangwei, C. Jing, The magnetic and microwave absorbing properties of the as spun Nd-Fe-Co-B nanocomposites, *J. Magn. Magn. Mater.* 443 (2017) 85–88. doi:10.1016/j.jmmm.2017.07.023.
- [2] A.G. Abraham, A. Manikandan, E. Manikandan, S. Vadivel, S.K. Jaganathan, A. Baykal, P.S. Renganathan, Enhanced magneto-optical and photo-catalytic properties of transition metal cobalt ( $\text{Co}^{2+}$  ions) doped spinel  $\text{MgFe}_2\text{O}_4$  ferrite nanocomposites, *J. Magn. Magn. Mater.* 452 (2018) 380–388. doi:10.1016/j.jmmm.2018.01.001.
- [3] A. Manikandan, E. Manikandan, B. Meenatchi, S. Vadivel, S.K. Jaganathan, R. Ladchumananandasivam, M. Henini, M. Maaza, J.S. Aanand, Rare earth element (REE) lanthanum doped zinc oxide ( $\text{La:ZnO}$ ) nanomaterials: Synthesis structural optical and antibacterial studies, *J. Alloys Compd.* 723 (2017) 1155–1161. doi:10.1016/j.jallcom.2017.06.336.
- [4] V. Umapathy, A. Manikandan, S. Arul Antony, P. Ramu, P. Neeraja, Structure, morphology and opto-magnetic properties of  $\text{Bi}_2\text{MoO}_6$  nano-photocatalyst synthesized by sol-gel method, *Trans. Nonferrous Met. Soc. China (English Ed.)* 25 (2015) 3271–3278. doi:10.1016/S1003-6326(15)63948-6.
- [5] D.K. Manimegalai, A. Manikandan, S. Moortheswaran, S.A. Antony, Magneto-Optical and Photocatalytic Properties of Magnetically Recyclable  $\text{Mn}_x\text{Zn}_{1-x}\text{S}$  ( $x = 0.0, 0.3, \text{ and } 0.5$ ) Nanocatalysts, *J. Supercond. Nov. Magn.* 28 (2015) 2755–2766. doi:10.1007/s10948-015-3089-3.
- [6] M.Z. Khan, I.H. Gul, H. Anwar, S. Ameer, A.N. Khan, A.A. Khurram, K. Nadeem, M. Mumtaz, Massive dielectric properties enhancement of  $\text{MWCNTs/CoFe}_2\text{O}_4$  nanohybrid for super capacitor applications, *J. Magn. Magn. Mater.* 424 (2017) 382–387. doi:10.1016/j.jmmm.2016.10.087.
- [7] A. Sun, L. Xie, D. Wang, Z. Wu, Enhanced energy storage performance from Co-decorated  $\text{MoS}_2$  nanosheets as supercapacitor electrode materials, *Ceram. Int.* (2018). doi:10.1016/j.ceramint.2018.04.113.
- [8] N.N. Reddy, S. Ravindra, N.M. Reddy, V. Rajinikanth, K.M. Raju, V.S. Vallabhapurapu, Temperature responsive hydrogel magnetic nanocomposites for hyperthermia and metal extraction applications, *J. Magn. Magn. Mater.* 394 (2015) 237–244. doi:10.1016/j.jmmm.2015.06.065.
- [9] G. Wang, Y. Ma, L. Zhang, J. Mu, Z. Zhang, X. Zhang, H. Che, Y. Bai, J. Hou, Facile synthesis of manganese ferrite/graphene oxide nanocomposites for controlled targeted drug delivery, *J. Magn. Magn. Mater.* 401 (2016) 647–650. doi:10.1016/j.jmmm.2015.10.096.

- [10] H. Fan, B. Li, Z. Shi, L. Zhao, K. Wang, D. Qiu, A fibrous morphology silica-CoFe<sub>2</sub>O<sub>4</sub> nanocarrier for anti-cancer drug delivery, *Ceram. Int.* 44 (2018) 2345–2350. doi:10.1016/j.ceramint.2017.10.201.
- [11] D.N. Thanh, P. Novák, J. Vejpravova, H.N. Vu, J. Lederer, T. Munshi, Removal of copper and nickel from water using nanocomposite of magnetic hydroxyapatite nanorods, *J. Magn. Magn. Mater.* 456 (2018) 451–460. doi:10.1016/j.jmmm.2017.11.064.
- [12] A. Manikandan, A. Saravanan, S.A. Antony, M. Bououdina, One-Pot Low Temperature Synthesis and Characterization Studies of Nanocrystalline  $\alpha$ -Fe<sub>2</sub>O<sub>3</sub>, Based Dye Sensitized Solar Cells, *J. Nanosci. Nanotechnol.* 15 (2015) 4358–4366. doi:10.1166/jnn.2015.9804.
- [13] A. Manikandan, J.J. Vijaya, L.J. Kennedy, Structural, Optical and Magnetic Properties of Porous  $\alpha$ -Fe<sub>2</sub>O<sub>3</sub>; Nanostructures Prepared by Rapid Combustion Method, *J. Nanosci. Nanotechnol.* 13 (2013) 2986–2992. doi:10.1166/jnn.2013.7402.
- [14] R.D. Ambashta, M. Sillanpää, Water purification using magnetic assistance: A review, *J. Hazard. Mater.* 180 (2010) 38–49. doi:10.1016/J.JHAZMAT.2010.04.105.
- [15] J. Zhu, S. Wei, M. Chen, H. Gu, S.B. Rapole, S. Pallavkar, T.C. Ho, J. Hopper, Z. Guo, Magnetic nanocomposites for environmental remediation, *Adv. Powder Technol.* 24 (2013) 459–467. doi:10.1016/J.APT.2012.10.012.
- [16] M. Brigante, E. Pecini, M. Avena, Magnetic mesoporous silica for water remediation: Synthesis, characterization and application as adsorbent of molecules and ions of environmental concern, *Microporous Mesoporous Mater.* 230 (2016) 1–10. doi:10.1016/J.MICROMESO.2016.04.032.
- [17] C. Tang, Y.H. Huang, H. Zeng, Z. Zhang, Reductive removal of selenate by zero-valent iron: The roles of aqueous Fe<sup>2+</sup> and corrosion products, and selenate removal mechanisms, *Water Res.* 67 (2014) 166–174. doi:10.1016/J.WATRES.2014.09.016.
- [18] L. Ling, B. Pan, W. Zhang, Removal of selenium from water with nanoscale zero-valent iron: Mechanisms of intraparticle reduction of Se(IV), *Water Res.* 71 (2015) 274–281. doi:10.1016/J.WATRES.2015.01.002.
- [19] C. Tang, Y. Huang, Z. Zhang, J. Chen, H. Zeng, Y.H. Huang, Rapid removal of selenate in a zero-valent iron/Fe<sub>3</sub>O<sub>4</sub>/Fe<sup>2+</sup> synergetic system, *Appl. Catal. B Environ.* 184 (2016) 320–327. doi:10.1016/J.APCATB.2015.11.045.
- [20] Y. Sun, S.S. Chen, D.C.W. Tsang, N.J.D. Graham, Y.S. Ok, Y. Feng, X.-D. Li, Zero-valent iron for the abatement of arsenate and selenate from flowback water of hydraulic fracturing, *Chemosphere.* 167 (2017) 163–170. doi:10.1016/J.CHEMOSPHERE.2016.09.120.

- [21] Z. Ma, C. Shan, J. Liang, M. Tong, Efficient adsorption of Selenium(IV) from water by hematite modified magnetic nanoparticles, *Chemosphere*. 193 (2018) 134–141. doi:10.1016/J.CHEMOSPHERE.2017.11.005.
- [22] S.A. Hosseini, A. Niaei, D. Salari, S.R. Nabavi, Nanocrystalline  $AMn_2O_4$  (A = Co, Ni, Cu) spinels for remediation of volatile organic compounds - Synthesis, characterization and catalytic performance, *Ceram. Int.* 38 (2012) 1655–1661. doi:10.1016/j.ceramint.2011.09.057.
- [23] A.A. Mirzaei, A.B. babaei, M. Galavy, A. Youssefi, A silica supported Fe–Co bimetallic catalyst prepared by the sol/gel technique: Operating conditions, catalytic properties and characterization, *Fuel Process. Technol.* 91 (2010) 335–347. doi:10.1016/J.FUPROC.2009.11.005.
- [24] N.D. Meeks, V. Smuleac, C. Stevens, D. Bhattacharyya, Iron-Based Nanoparticles for Toxic Organic Degradation: Silica Platform and Green Synthesis, *Ind. Eng. Chem. Res.* 51 (2012) 9581–9590. doi:10.1021/ie301031u.
- [25] K. Keyvanloo, M.K. Mardkhe, T.M. Alam, C.H. Bartholomew, B.F. Woodfield, W.C. Hecker, Supported Iron Fischer–Tropsch Catalyst: Superior Activity and Stability Using a Thermally Stable Silica-Doped Alumina Support, *ACS Catal.* 4 (2014) 1071–1077. doi:10.1021/cs401242d.
- [26] B. Liu, Z. Zhang, Catalytic Conversion of Biomass into Chemicals and Fuels over Magnetic Catalysts, *ACS Catal.* 6 (2016) 326–338. doi:10.1021/acscatal.5b02094.
- [27] C. Ragupathi, J. Judith Vijaya, S. Narayanan, S.K. Jesudoss, L. John Kennedy, Highly selective oxidation of benzyl alcohol to benzaldehyde with hydrogen peroxide by cobalt aluminate catalysis: A comparison of conventional and microwave methods, *Ceram. Int.* 41 (2015) 2069–2080. doi:10.1016/j.ceramint.2014.10.002.
- [28] S. Jauhar, S. Singhal, Substituted cobalt nano-ferrites ,  $CoM_xFe_{2-x}O_4$  (M =  $Cr^{3+}$ ,  $Ni^{2+}$ ,  $Cu^{2+}$ ,  $Zn^{2+}$ ;  $0.2 \leq x \leq 1.0$  ) as heterogeneous catalysts for modified Fenton's reaction, *Ceram. Int.* 40 (2014) 11845–11855.
- [29] A.K. Gupta, M. Gupta, Synthesis and surface engineering of iron oxide nanoparticles for biomedical applications, *Biomaterials*. 26 (2005) 3995–4021. doi:10.1016/J.BIOMATERIALS.2004.10.012.
- [30] M. Chao, L. Chuanyan, H. Nongyue, W. Fang, M. Ningning, Z. Liming, L. Zhuoxuan, A. Zeeshan, X. Zhijiang, L. Xiaolong, L. Gaofeng, L. Hongna, D. Yan, X. Lijian, W. Zhifei, Preparation and Characterization of Monodisperse Core–Shell  $Fe_3O_4@SiO_2$  Microspheres and Its Application for Magnetic Separation of Nucleic Acids from *E. coli* BL21, *J. Biomed. Nanotechnol.* 8 (2012) 1000–1005. doi:https://doi.org/10.1166/jbnn.2012.1454.
- [31] R. Sharma, P. Thakur, M. Kumar, P.B. Barman, P. Sharma, V. Sharma, Enhancement in A-B super-exchange interaction with  $Mn^{2+}$  substitution in Mg-

- Zn ferrites as a heating source in hyperthermia applications, *Ceram. Int.* 43 (2017) 13661–13669. doi:10.1016/j.ceramint.2017.07.076.
- [32] L. Muzquiz-Ramos, EM and Guerrero-Chavez, V and Macias-Martinez, BI and Lopez-Badillo, CM and Garcia-Cerda, Synthesis and characterization of maghemite nanoparticles for hyperthermia, *Ceram. Int.* 41 (2015) 397–402.
- [33] M. Zhao, S. Fan, J. Liang, Y. Liu, Y. Li, J. Chen, S. Chen, Synthesis of mesoporous grooved  $\text{ZnFe}_2\text{O}_4$  nanobelts as peroxidase mimetics for improved enzymatic biosensor, *Ceram. Int.* 41 (2015) 10400–10405. doi:10.1016/j.ceramint.2015.04.080.
- [34] S. Esposito, A. Marocco, B. Bonelli, M. Pansini, Produzione di materiali compositi metallo-ceramici nano strutturati da precursori zeolitici, MI 2014 A 000522, 2014.
- [35] S. Esposito, A. Marocco, B. Bonelli, M. Pansini, Production of magnetic metal nanoparticles embedded in a silica-alumina matrix, WO 2015/145230 A1, 2015.
- [36] A. Marocco, G. Dell’Agli, S. Esposito, M. Pansini, Metal-ceramic composite materials from zeolite precursor, *Solid State Sci.* 14 (2012) 394–400. doi:10.1016/J.SOLIDSTATESCIENCES.2012.01.006.
- [37] A.T. Ravichandran, J. Srinivas, R. Karthick, A. Manikandan, A. Baykal, Facile combustion synthesis, structural, morphological, optical and antibacterial studies of  $\text{Bi}_{1-x}\text{Al}_x\text{FeO}_3$  ( $0.0 \leq x \leq 0.15$ ) nanoparticles, *Ceram. Int.* 44 (2018) 13247–13252. doi:10.1016/j.ceramint.2018.04.153.
- [38] A. Manikandan, S.A. Antony, A Novel Approach for the Synthesis and Characterization Studies of  $\text{Mn}^{2+}$ -Doped CdS Nanocrystals by a Facile Microwave-Assisted Combustion Method, *J. Supercond. Nov. Magn.* 27 (2014) 2725–2733. doi:10.1007/s10948-014-2634-9.
- [39] S. Jayasree, A. Manikandan, A.M.U. Mohideen, C. Barathiraja, S.A. Antony, Comparative Study of Combustion Methods, Opto-Magnetic and Catalytic Properties of Spinel  $\text{CoAl}_2\text{O}_4$  Nano-and Microstructures, *Adv. Sci. Eng. Med.* 7 (2015) 672–682. doi:10.1166/ase.2015.1750.
- [40] M. Pansini, G. Dell’Agli, A. Marocco, P.A.P.A. Netti, E. Battista, V. Lettera, P. Vergara, P. Allia, B. Bonelli, P. Tiberto, G. Barrera, G. Alberto, G. Martra, R. Arletti, S. Esposito, others, Preparation and Characterization of Magnetic and Porous Metal-Ceramic Nanocomposites from a Zeolite Precursor and Their Application for DNA Separation, *J. Biomed. Nanotechnol.* 13 (2017) 337–348. doi:10.1166/jbn.2017.2345.
- [41] M. Pansini, F. Sannino, A. Marocco, P. Allia, P. Tiberto, G. Barrera, M. Polisi, E. Battista, P.A. Netti, S. Esposito, Novel process to prepare magnetic metal-ceramic nanocomposites from zeolite precursor and their use as adsorbent of agrochemicals from water, *J. Environ. Chem. Eng.* 6 (2018).

- doi:10.1016/j.jece.2017.12.030.
- [42] S. Esposito, G. Dell'Agli, A. Marocco, B. Bonelli, P. Allia, P. Tiberto, G. Barrera, M. Manzoli, R. Arletti, M. Pansini, Magnetic metal-ceramic nanocomposites obtained from cation-exchanged zeolite by heat treatment in reducing atmosphere, *Microporous Mesoporous Mater.* 268 (2018) 131–143. doi:10.1016/J.MICROMESO.2018.04.024.
- [43] A. Marocco, M. Pansini, G. Dell'Agli, S. Esposito, Parameters Expediting the Thermal Conversion of Ba-Exchanged Zeolite A to Monoclinic Celsian, *Adv. Mater. Sci. Eng.* 2010 (2010) 1–8. doi:10.1155/2010/683429.
- [44] A. Marocco, G. Dell'Agli, S. Esposito, M. Pansini, The role of residual  $\text{Na}^+$  and  $\text{Li}^+$  on the thermal transformation of Ba-exchanged zeolite A, *Solid State Sci.* 13 (2011) 1143–1151. doi:10.1016/J.SOLIDSTATESCIENCES.2011.01.002.
- [45] S. Esposito, A. Marocco, G. Dell'Agli, B. De Gennaro, M. Pansini, Relationships between the water content of zeolites and their cation population, *Microporous Mesoporous Mater.* 202 (2015) 36–43. doi:10.1016/J.MICROMESO.2014.09.041.
- [46] D. Caruntu, G. Caruntu, C.J. O'Connor, Magnetic properties of variable-sized  $\text{Fe}_3\text{O}_4$  nanoparticles synthesized from non-aqueous homogeneous solutions of polyols, *J. Phys. D. Appl. Phys.* 40 (2007) 5801–5809. doi:10.1088/0022-3727/40/19/001.
- [47] S. Araújo-Barbosa, M.A. Morales, Magnetic studies of nickel hydride nanoparticles embedded in chitosan matrix, *J. Magn. Magn. Mater.* 441 (2017) 702–709. doi:10.1016/j.jmmm.2017.06.079.
- [48] E. Hema, A. Manikandan, M. Gayathri, M. Durka, S.A. Antony, B.R. Venkatraman, The Role of  $\text{Mn}^{2+}$ -Doping on Structural, Morphological, Optical, Magnetic and Catalytic Properties of Spinel  $\text{ZnFe}_2\text{O}_4$  Nanoparticles, *J. Nanosci. Nanotechnol.* 16 (2016) 5929–5943. doi:10.1166/jnn.2016.11037.
- [49] S. Suguna, S. Shankar, S.K. Jaganathan, A. Manikandan, Novel Synthesis of Spinel  $\text{Mn}_x\text{Co}_{1-x}\text{Al}_2\text{O}_4$  ( $x = 0.0$  to  $1.0$ ) Nanocatalysts: Effect of  $\text{Mn}^{2+}$  Doping on Structural, Morphological, and Opto-Magnetic Properties, *J. Supercond. Nov. Magn.* 30 (2017) 691–699. doi:10.1007/s10948-016-3866-7.
- [50] S. Asiri, M. Sertkol, S. Guner, H. Gungunes, K.M. Batoo, T.A. Saleh, H. Sozeri, M.A. Almessiere, A. Manikandan, A. Baykal, Hydrothermal synthesis of  $\text{Co}_y\text{Zn}_y\text{Mn}_{1-2y}\text{Fe}_2\text{O}_4$  nanoferrites: Magneto-optical investigation, *Ceram. Int.* 44 (2018) 5751–5759. doi:10.1016/j.ceramint.2017.12.233.
- [51] G. Padmapriya, A. Manikandan, V. Krishnasamy, S.K. Jaganathan, S.A. Antony, Enhanced Catalytic Activity and Magnetic Properties of Spinel  $\text{Mn}_x\text{Zn}_{1-x}\text{Fe}_2\text{O}_4$  ( $0.0 \leq x \leq 1.0$ ) Nano-Photocatalysts by Microwave Irradiation Route, *J. Supercond. Nov. Magn.* 29 (2016) 2141–2149. doi:10.1007/s10948-016-3527-x.

- [52] E. Hema, A. Manikandan, P. Karthika, M. Durka, S.A. Antony, B.R. Venkatraman, Magneto-Optical Properties of Reusable Spinel  $\text{Ni}_x\text{Mg}_{1-x}\text{Fe}_2\text{O}_4$  ( $0.0 \leq x \leq 1.0$ ) Nano-Catalysts, J. Nanosci. Nanotechnol. 16 (2016) 7325–7336. doi:10.1166/jnn.2016.11109.
- [53] A.G. Abraham, A. Manikandan, E. Manikandan, S.K. Jaganathan, A. Baykal, P.S. Renganathan, Enhanced Opto-Magneto Properties of  $\text{Ni}_x\text{Mg}_{1-x}\text{Fe}_2\text{O}_4$  ( $0.0 \leq x \leq 1.0$ ) Ferrites Nano-Catalysts, J. Nanoelectron. Optoelectron. 12 (2017) 1326–1333. doi:10.1166/jno.2017.2299.
- [54] Y. Slimani, H. Güngüneş, M. Nawaz, A. Manikandan, H.S. El Sayed, M.A. Almessiere, H. Sözeri, S.E. Shirsath, I. Ercan, A. Baykal, Magneto-optical and microstructural properties of spinel cubic copper ferrites with Li-Al co-substitution, Ceram. Int. 44 (2018) 14242–14250. doi:10.1016/j.ceramint.2018.05.028.
- [55] S.D. Tiwari, K.P. Rajeev, Effect of distributed particle magnetic moments on the magnetization of NiO nanoparticles, Solid State Commun. 152 (2012) 1080–1083. doi:10.1016/j.ssc.2012.03.003.
- [56] C.P. Poole, V.G. Bar'iahtar, Encyclopedic dictionary of condensed matter physics. Volume 1, A-M, Elsevier, 2004.
- [57] A.N. Mlinar, G.B. Baur, G.G. Bong, A. Getsoian, A.T. Bell, Propene oligomerization over Ni-exchanged Na-X zeolites, J. Catal. 296 (2012) 156–164. doi:10.1016/j.jcat.2012.09.010.
- [58] M. Sano, T. Maruo, H. Yamatera, M. Suzuki, Y. Saito, N.Y. Zeolite, EXAFS studies on the origin of high catalytic activity in nickel Y zeolite, J. Am. Chem. Soc. 109 (1987) 52–55. doi:10.1021/ja00235a008.
- [59] A. Luengnaruemitchai, A. Kaengsilalai, Activity of different zeolite-supported Ni catalysts for methane reforming with carbon dioxide, Chem. Eng. J. 144 (2008) 96–102. doi:10.1016/j.cej.2008.05.023.
- [60] A. Cheetham, D. Hope, Magnetic ordering and exchange effects in the antiferromagnetic solid solutions  $\text{Mn}_x\text{Ni}_{1-x}\text{O}$ , Phys. Rev. B. 27 (1983) 6964–6967. doi:10.1103/PhysRevB.27.6964.
- [61] J.B. Yi, J. Ding, Y.P. Feng, G.W. Peng, G.M. Chow, Y. Kawazoe, B.H. Liu, J.H. Yin, S. Thongmee, Size-dependent magnetism and spin-glass behavior of amorphous NiO bulk, clusters, and nanocrystals: Experiments and first-principles calculations, Phys. Rev. B - Condens. Matter Mater. Phys. 76 (2007) 2–6. doi:10.1103/PhysRevB.76.224402.
- [62] S. Matsuo, S. Satou, M. Suzuki, M. Sano, H. Nakano, Magnetic properties of small nickel oxide clusters enclosed in Y-zeolite, Atoms, Mol. Clust. 285 (1991) 281–285.



- [63] N. Jaeger, U. Melville, R. Nowak, H. Schröbbers, G. Schulz-Ekloff, The Influence of Calcium Ions on the Properties of Nickel Faujasite Catalysts for the Hydrogenation of Carbon Monoxide, *Stud. Surf. Sci. Catal.* 5 (1980) 335–340. doi:10.1016/S0167-2991(08)64895-8.
- [64] M.D. Mukadam, S.M. Yusuf, R. Sasikala, T. Ni, Magnetic properties of Ni<sup>2+</sup> clusters in NaY zeolite, *J. Appl. Phys.* 103902 (2007) 1–5. doi:10.1063/1.2815624.
- [65] A.L. Barra, A. Caneschi, A. Cornia, F.F. De Biani, D. Gatteschi, Single-Molecule Magnet Behavior of a Tetranuclear Iron ( III ) Complex . The Origin of Slow Magnetic Relaxation in Iron ( III ) Clusters, *J. Am. Chem. Soc.* 121 (1999) 5302–5310. doi:10.1021/ja9818755.
- [66] M. Hagiwara, K. Minami, Y. Narumi, Magnetic Properties of a Quantum Ferrimagnet : NiCu(pba)(D<sub>2</sub>O)<sub>3</sub> 2D<sub>2</sub>O, *J. Phys. Soc. Jpn.* 67 (1998) 2209–2211. doi:10.1143/JPSJ.67.2209.
- [67] H.Z. Kou, S. Gao, C.H. Li, D.Z. Liao, B.C. Zhou, R.J. Wang, Y. Li, Characterization of a soluble molecular magnet: Unusual magnetic behavior of cyano-bridged Gd(III)-Cr(III) complexes with one-dimensional and nanoscaled square structures, *Inorg. Chem.* 41 (2002) 4756–4762. doi:10.1021/ic025704j.
- [68] V.S. Zagaynova, T.L. Makarova, N.G. Spitsina, D.W. Boukhvalov, Synthesis and Magnetic Properties of Mn<sub>12</sub>-Based Single Molecular Magnets with Benzene and Pentafluorobenzene Carboxylate Ligands, *J. Supercond. Nov. Magn.* 24 (2011) 855–859. doi:10.1007/s10948-010-1030-3.
- [69] W. Gong, H. Li, Z. Zhao, J. Chen, Ultrafine particles of Fe, Co, and Ni ferromagnetic metals, *J. Appl. Phys.* 69 (1991) 5119–5121. doi:10.1063/1.348144.
- [70] H. Mamiya, M. Ohnuma, I. Nakatani, T. Furubayashim, Extraction of blocking temperature distribution from zero-field-cooled and field-cooled magnetization curves, *IEEE Trans. Magn.* 41 (2005) 3394–3396. doi:10.1109/TMAG.2005.855205.
- [71] P. Allia, G. Barrera, P. Tiberto, T. Nardi, Y. Leterrier, M. Sangermano, Fe<sub>3</sub>O<sub>4</sub> nanoparticles and nanocomposites with potential application in biomedicine and in communication technologies: Nanoparticle aggregation, interaction, and effective magnetic anisotropy, *J. Appl. Phys.* 116 (2014). doi:10.1063/1.4895837.
- [72] J. Bartolome, S. Luis, F.J.F.. Fernández, eds., *Molecular Magnet*, Springer, 2014.
- [73] M. Knobel, W.C. Nunes, L.M. Socolovsky, E. De Biasi, J.M. Vargas, J.C. Denardin, Superparamagnetism and Other Magnetic Features in Granular Materials: A Review on Ideal and Real Systems, *J. Nanosci. Nanotechnol.* 8 (2008) 2836–2857. doi:10.1166/jnn.2008.15348.

- [74] J.M.D. Coey, Magnetism and Magnetic Materials, 2009.
- [75] S. Vitta, Nonlinear spin wave magnetization of solution synthesized Ni nanoparticles, J. Appl. Phys. 101 (2007). doi:10.1063/1.2710437.
- [76] Y. Ichiyanagi, Y. Kimishima, Magnetic and Structural Studies of Ni(OH)<sub>2</sub> Monolayered Nanoclusters, J. Appl. Phys. 35 (1996) 2140–2144.
- [77] G. Chaboussant, R. Basler, H.-U. Güdel, S. Ochsenbein, A. Parkin, S. Parsons, G. Rajaraman, A. Sieber, A. a Smith, G. a Timco, R.E.P. Winpenny, Nickel pivalate complexes: structural variations and magnetic susceptibility and inelastic neutron scattering studies., Dalton Trans. (2004) 2758–2766. doi:10.1039/b406112h.
- [78] J.S. Smart, The Néel Theory of Ferrimagnetism, Am. J. Phys. 23 (1955) 356–370. doi:10.1119/1.1934006.
- [79] J.B. Goodenough, Magnetism and the chemical bond, Interscience publisher, New York-London, 1963.

## Figures Captions

Fig. 1 – TEM images of NiA735C-12min (panel a) and NiA750C-0min (panel b) samples. Insets: Ni particle size distributions. Instrumental magnification: 100000X.

Fig. 2 – TEM images of NiX735C-12min (panel a) and NiX750C-0min (panel b) samples. Insets: Ni particle size distributions. Instrumental magnification: 100000X.

Fig. 3 – Temperature behavior of the hysteresis loops of ceramic nanocomposites obtained from different zeolite types. The insets show the low-field behavior.

Fig. 4 – Coercive field  $H_c$  as a function of measurement temperature for all studied samples.

Fig. 5 – Temperature dependence of the magnetization at  $H = 70$  kOe in all studied samples.

Fig. 6 – FC/ZFC magnetization curves of all studied samples measured under a field of 50 Oe between 2 and 300 K (in sample NiX750C-0min the starting temperature was 5.5 K). Top panel: nanocomposites resulting from precursor zeolite A; bottom panel: precursor zeolite X.

Fig. 7 – Magnification of the low-temperature structures of FC/ZFC curves measured in two selected nanocomposites; the displayed behavior is representative of all studied samples.

Fig. 8 – Low-temperature structures of all nanocomposites resulting after subtraction of the baseline (dashed lines in Fig. 7)

Fig. 9 – Reciprocal of the high-field susceptibility  $\chi_{HF}^{-1}$  as a function of temperature in metal-ceramic nanocomposites. Symbols: experimental data; red lines: high-temperature linear fit. See text for details.

Fig. 10 –  $\chi_{HF}T$  product as a function of temperature in metal-ceramic nanocomposites. Symbols: experimental data; red lines: expected behavior of  $\chi_{HF}T$  using  $\mu_{eff}$  (values on Table I); blue lines: expected behavior using  $\mu_{clust}$  (values in Table I).

Fig. 11 – Distribution of blocking temperatures of ferrimagnetic-like clusters in sample NiA750C-0min as obtained from the FC/ZFC curves of Fig. 8, panel (c).

Fig. 12 – Magnetization at  $H = 70$  kOe in a typical metal-ceramic nanocomposite. Full dots: experimental data; red dashed lines: high-temperature fitting curves using the Brillouin functions appropriate to  $Ni^{2+}$  ions with complete angular-momentum

quenching ( $B_{J=1}$ ) and without quenching ( $B_{J=4}$ ); blue full line: low-temperature fitting curve using Eq. (3) and the  $\mu_{\text{clust}}$  value reported in Table I.

**Table I**

Sample	$T_N$ (K)	$C$ ( $\text{cm}^3 \text{K g}^{-1}$ )	$f$	$n_{\text{eff}}$	$M_{\text{NP}}^*$ (emu/g)	$\mu_{\text{clust}}$ ( $\mu_B$ )
NiA735C-12min	13.5	$6.01 \times 10^{-4}$	0.46	2.25	35.4	9.17
NiX735C-12min	9.5	$8.99 \times 10^{-4}$	0.33	3.44	35.6	10.93
NiA750C- 0min	3.4	$9.99 \times 10^{-4}$	0.53	2.72	36.4	9.19
NiX750C- 0min	6.6	$7.10 \times 10^{-4}$	0.33	3.02	35.4	10.00

Table I: Paramagnetic-phase parameters in magnetic zeolite nanocomposites: Néel temperature  $T_N$ , Curie constant  $C$ , paramagnetic fraction  $f$  (from Ref. [42]), effective number of Bohr magnetons per single  $\text{Ni}^{2+}$  ion (at high temperature)  $n_{\text{eff}}$ , saturation magnetization of Ni nanoparticles (per unit mass of Ni) at  $T = 300 \text{ K}$   $M_{\text{NP}}^*$ , net magnetic moment of a cluster of  $\text{Ni}^{2+}$  ions  $\mu_{\text{clust}}$ .

**Table II**

Sample	$\langle T_B \rangle$ (K)	$U/k_B$ (K)		$U/k_B$ (meV)	
		$\tau_0 = 1 \times 10^{-7} \text{ s}$	$\tau_0 = 1 \times 10^{-9} \text{ s}$	$\tau_0 = 1 \times 10^{-7} \text{ s}$	$\tau_0 = 1 \times 10^{-9} \text{ s}$
NiA735C-12min	4.5	93	114	8.0	9.8
NiX735C-12min	3.0	62	76	5.4	6.6
NiA750C- 0min	3.3	68	84	5.9	7.2
NiX750C- 0min	-	< 93	<114	<8.0	<9.8

Table II: Mean value of the blocking temperature and estimates of the anisotropy energy barrier for magnetic moment reversal in Ni 15% zeolites containing magnetic clusters.

1  
2  
3  
4  
5  
6  
7  
8  
9  
10  
11  
12  
13  
14  
15  
16  
17  
18  
19  
20  
21  
22  
23  
24  
25  
26  
27  
28  
29  
30  
31  
32  
33  
34  
35  
36  
37  
38  
39  
40  
41  
42  
43  
44  
45  
46  
47  
48  
49  
50  
51  
52  
53  
54  
55  
56  
57  
58  
59  
60  
61  
62  
63  
64  
65

Figure 1  
[Click here to download high resolution image](#)

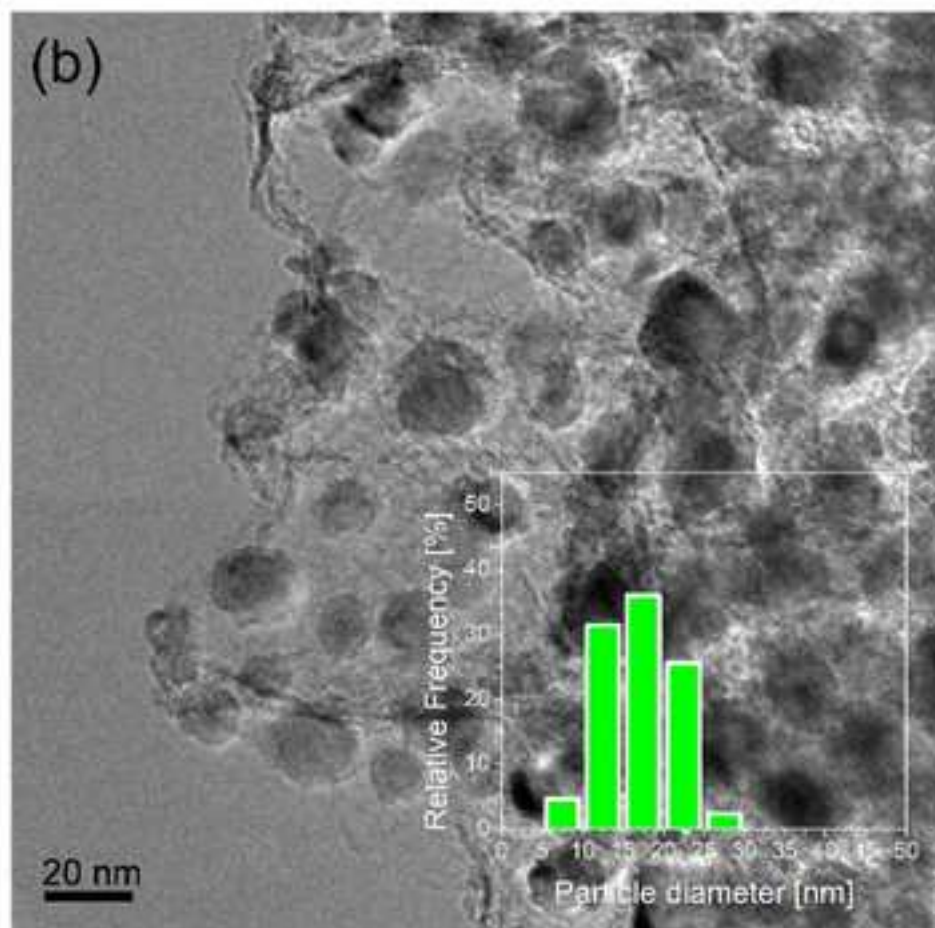
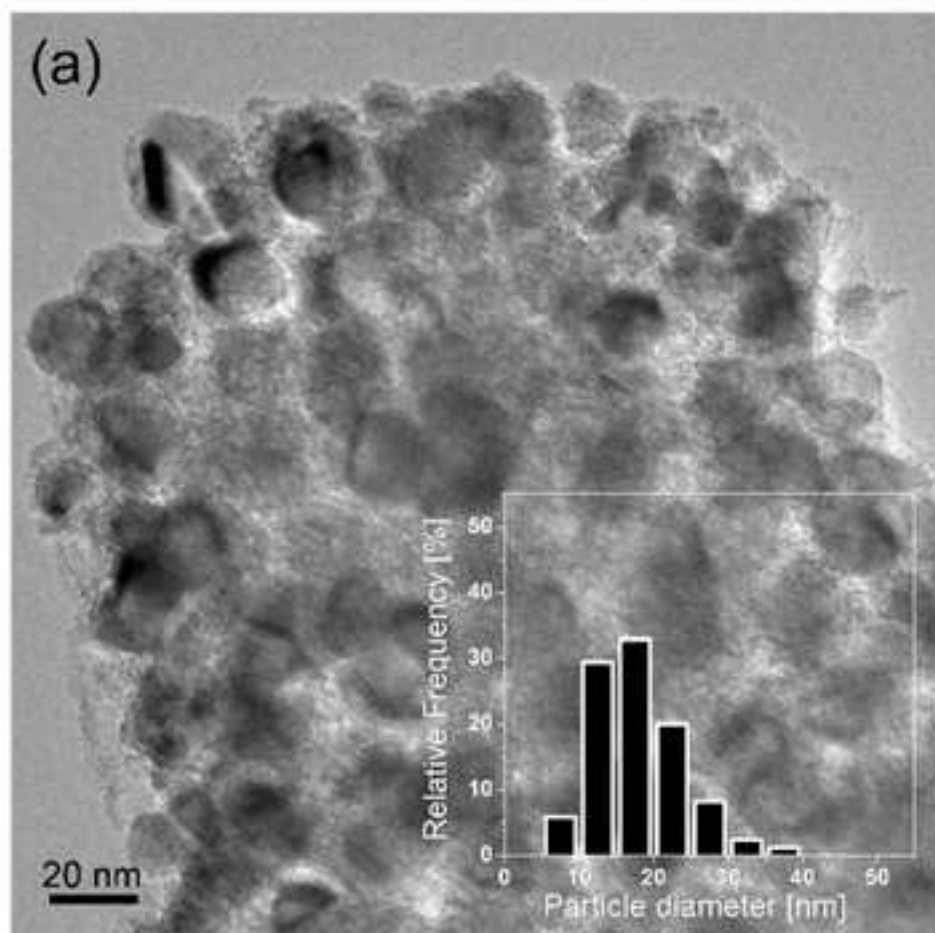


Figure 2  
[Click here to download high resolution image](#)

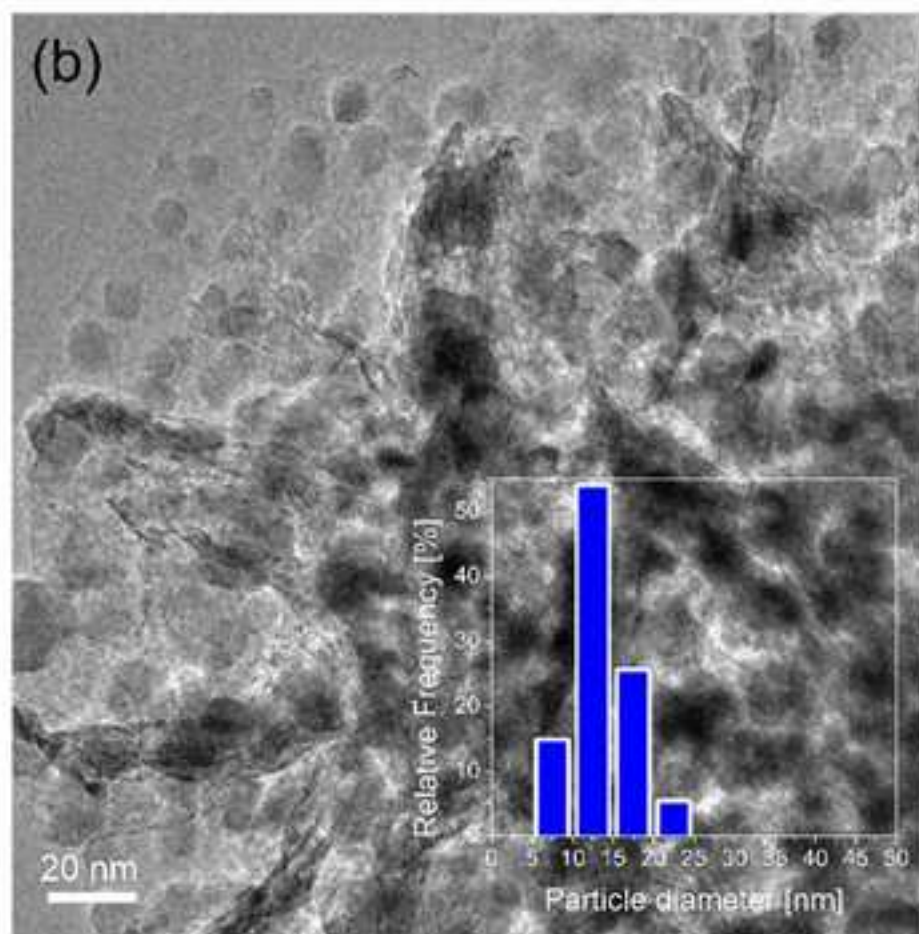
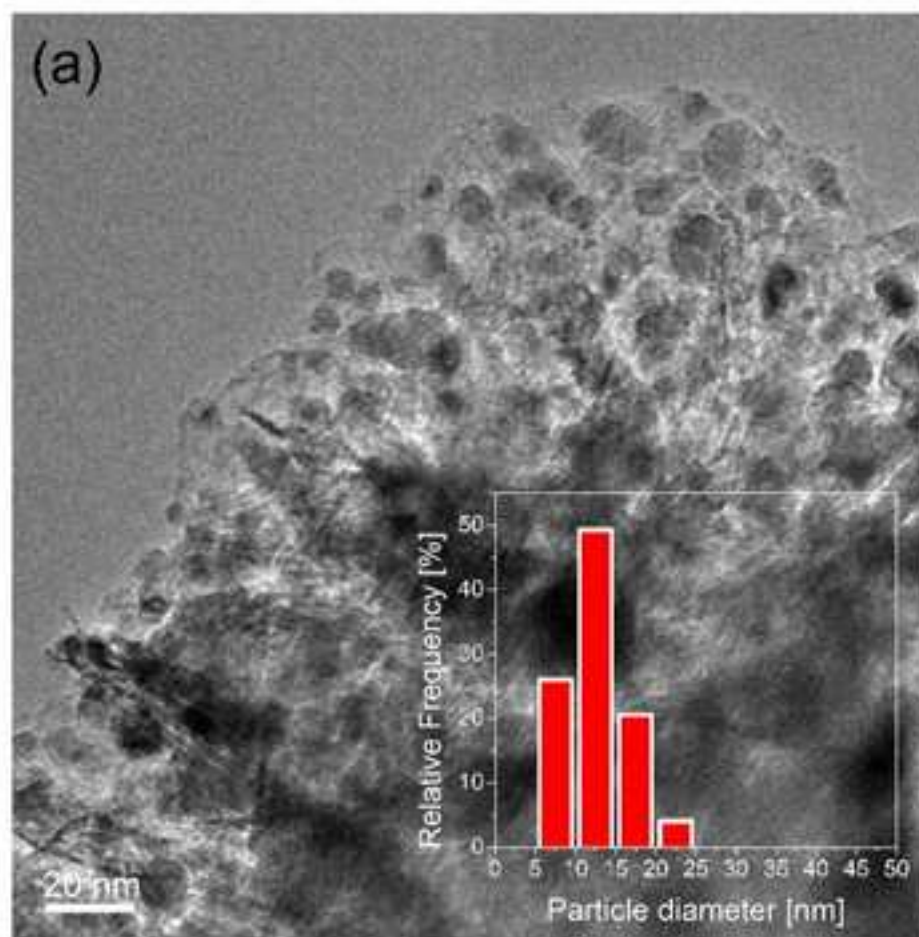




Figure 3

[Click here to download high resolution image](#)

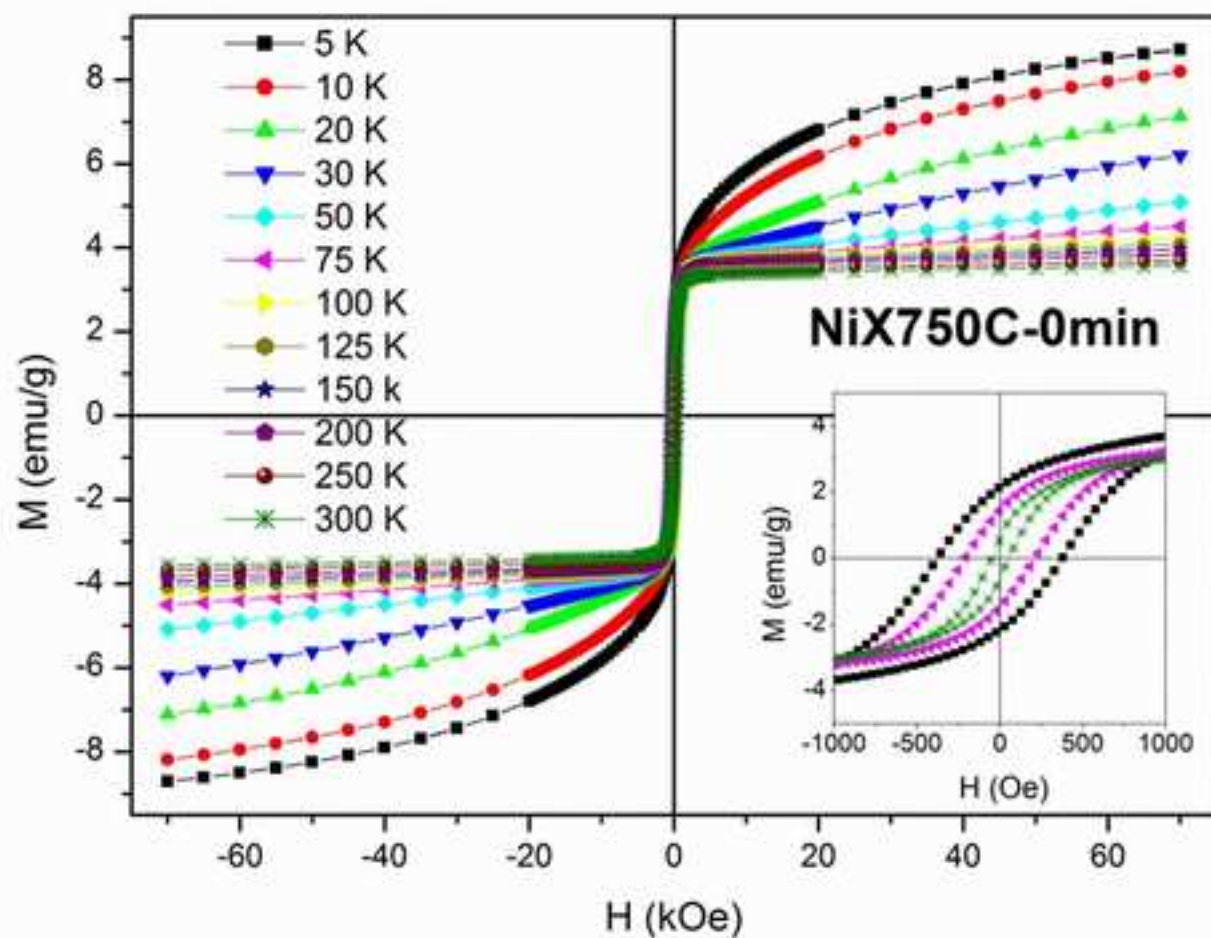
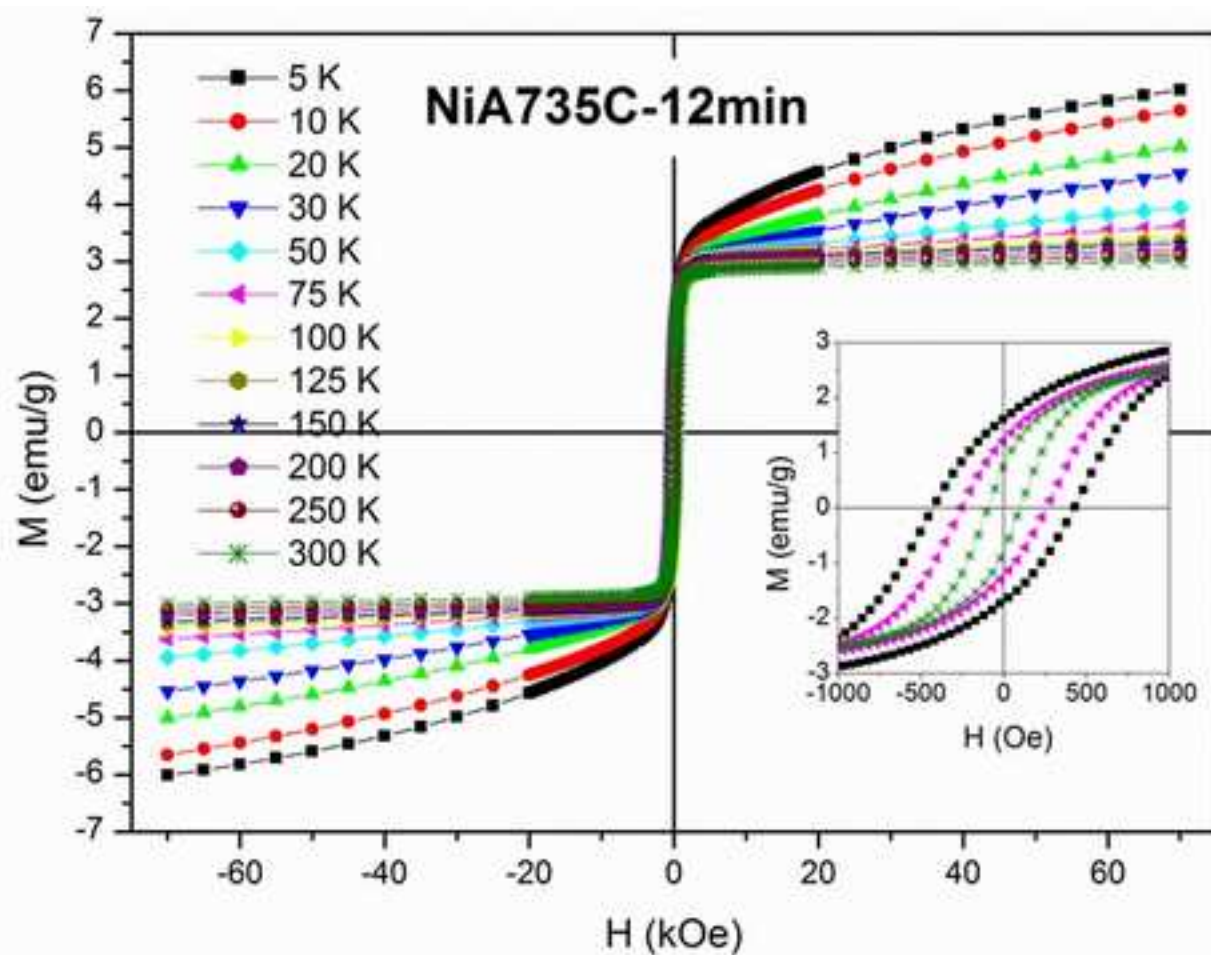




Figure 4  
[Click here to download high resolution image](#)

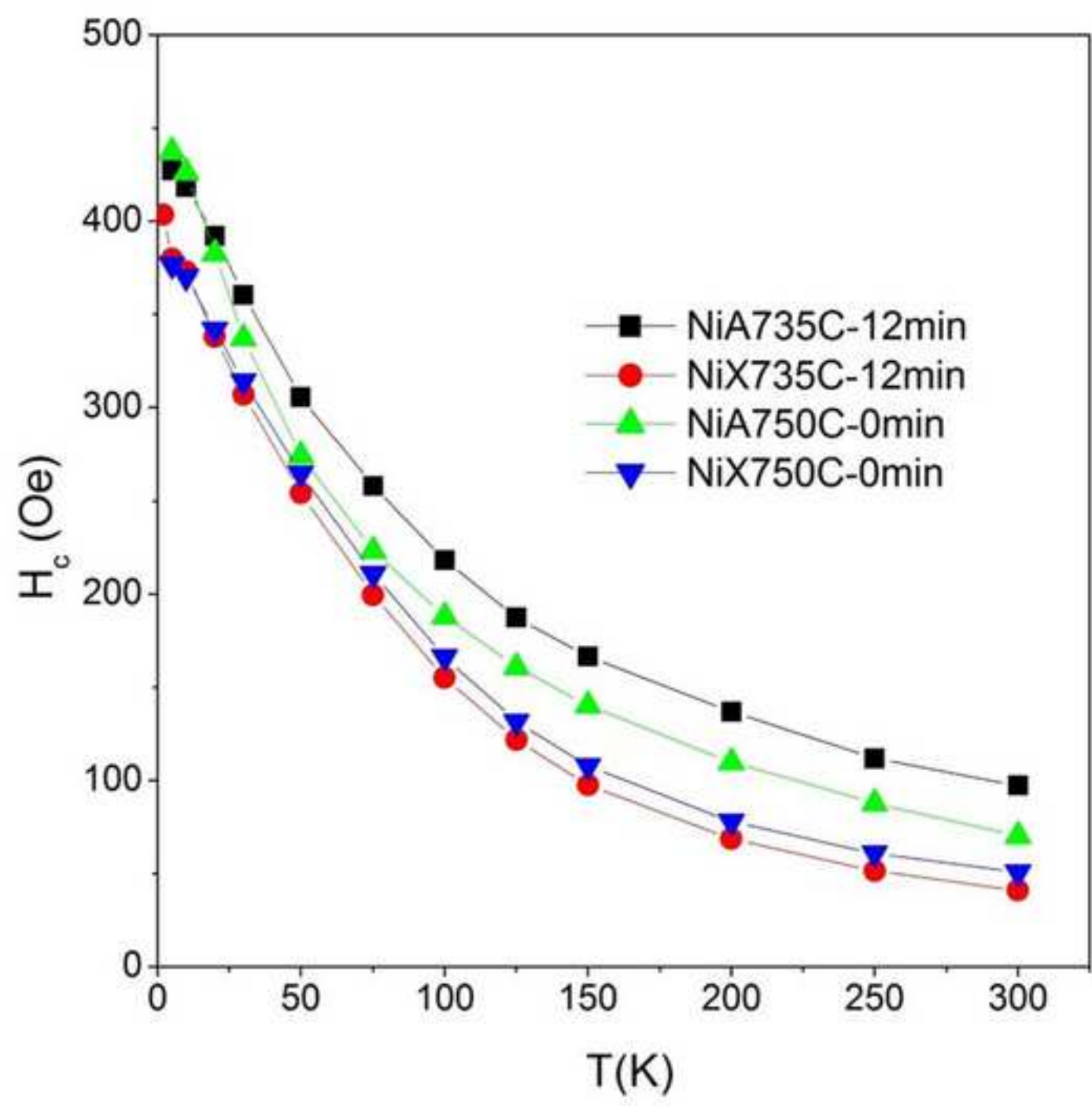


Figure 5  
[Click here to download high resolution image](#)

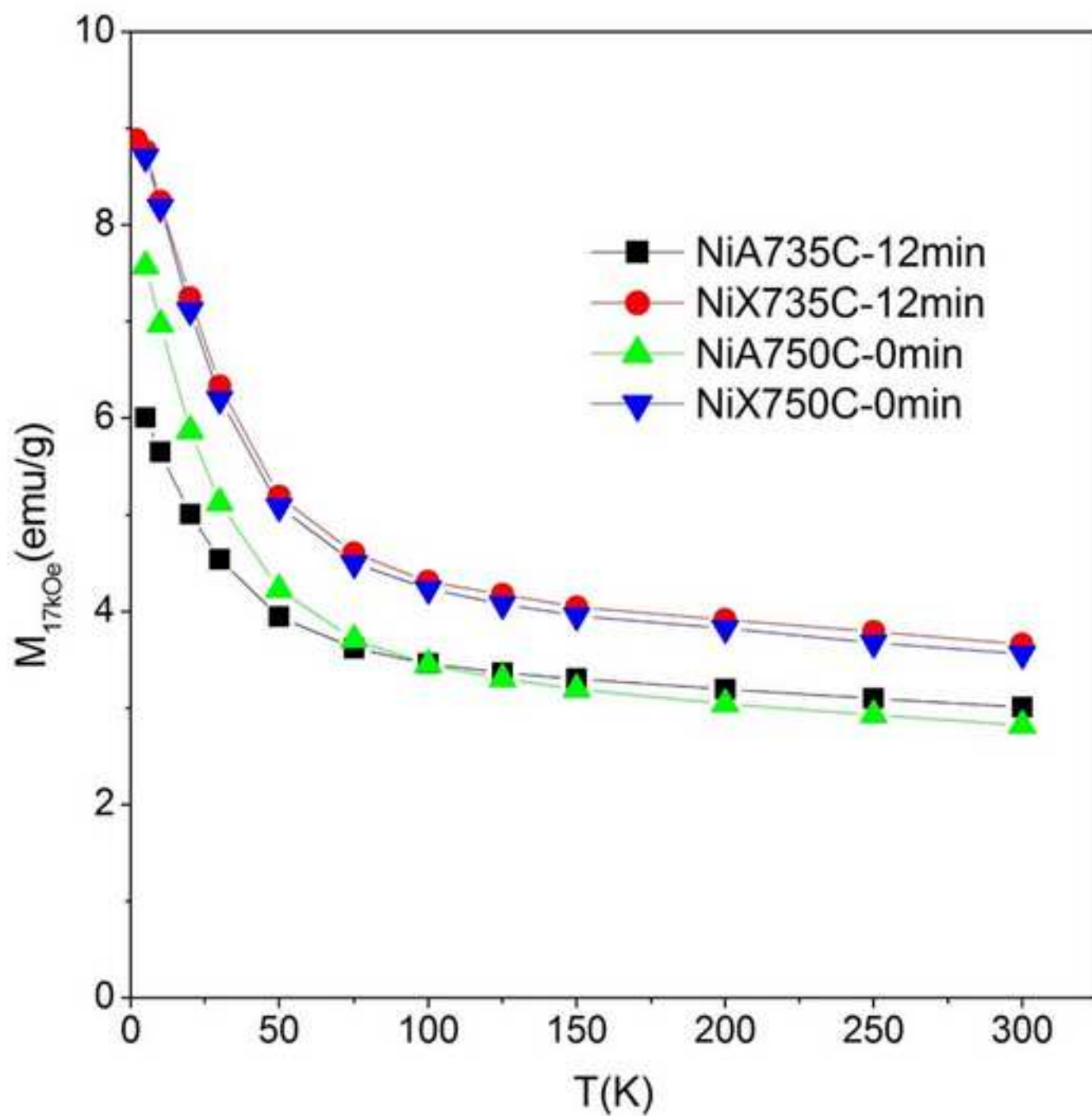


Figure 6  
[Click here to download high resolution image](#)

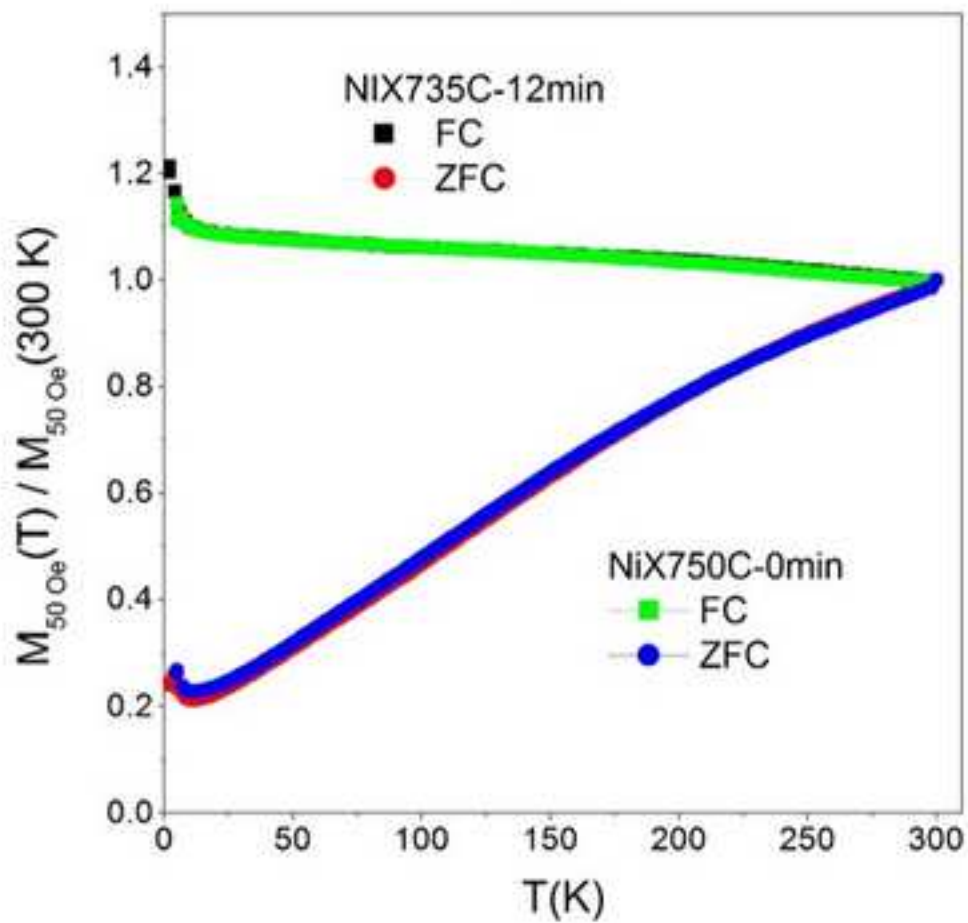
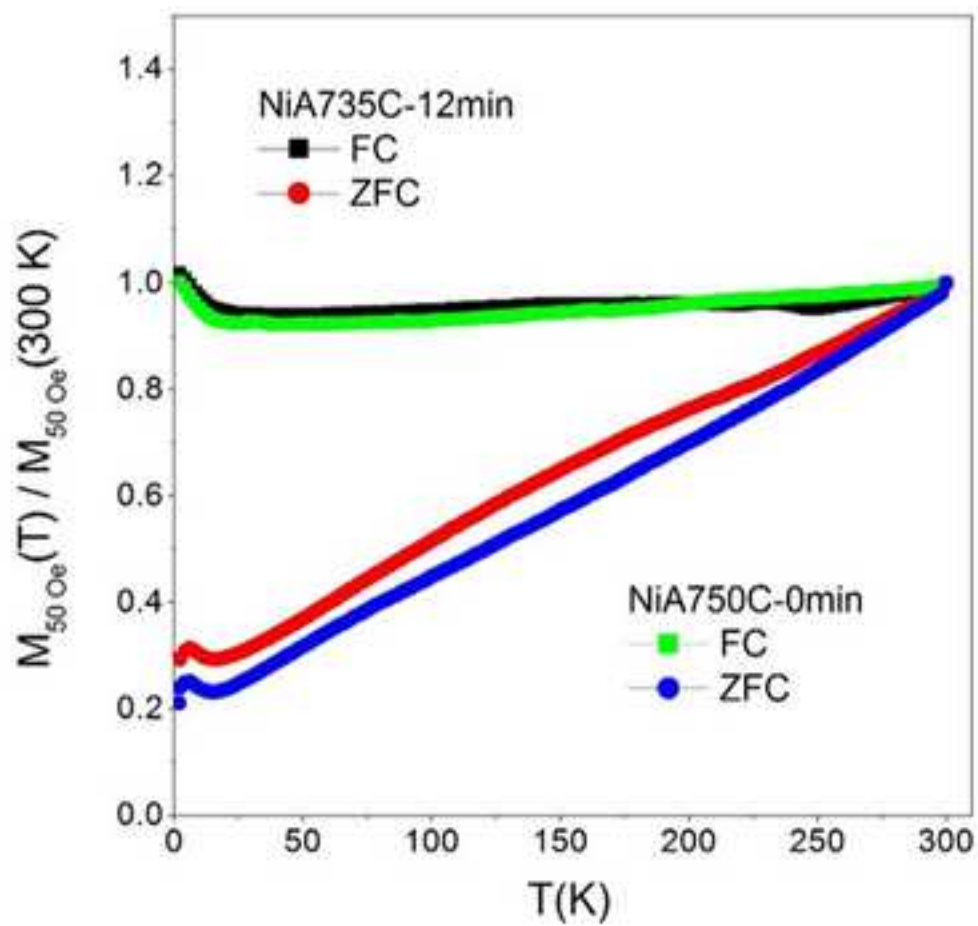


Figure 7  
[Click here to download high resolution image](#)

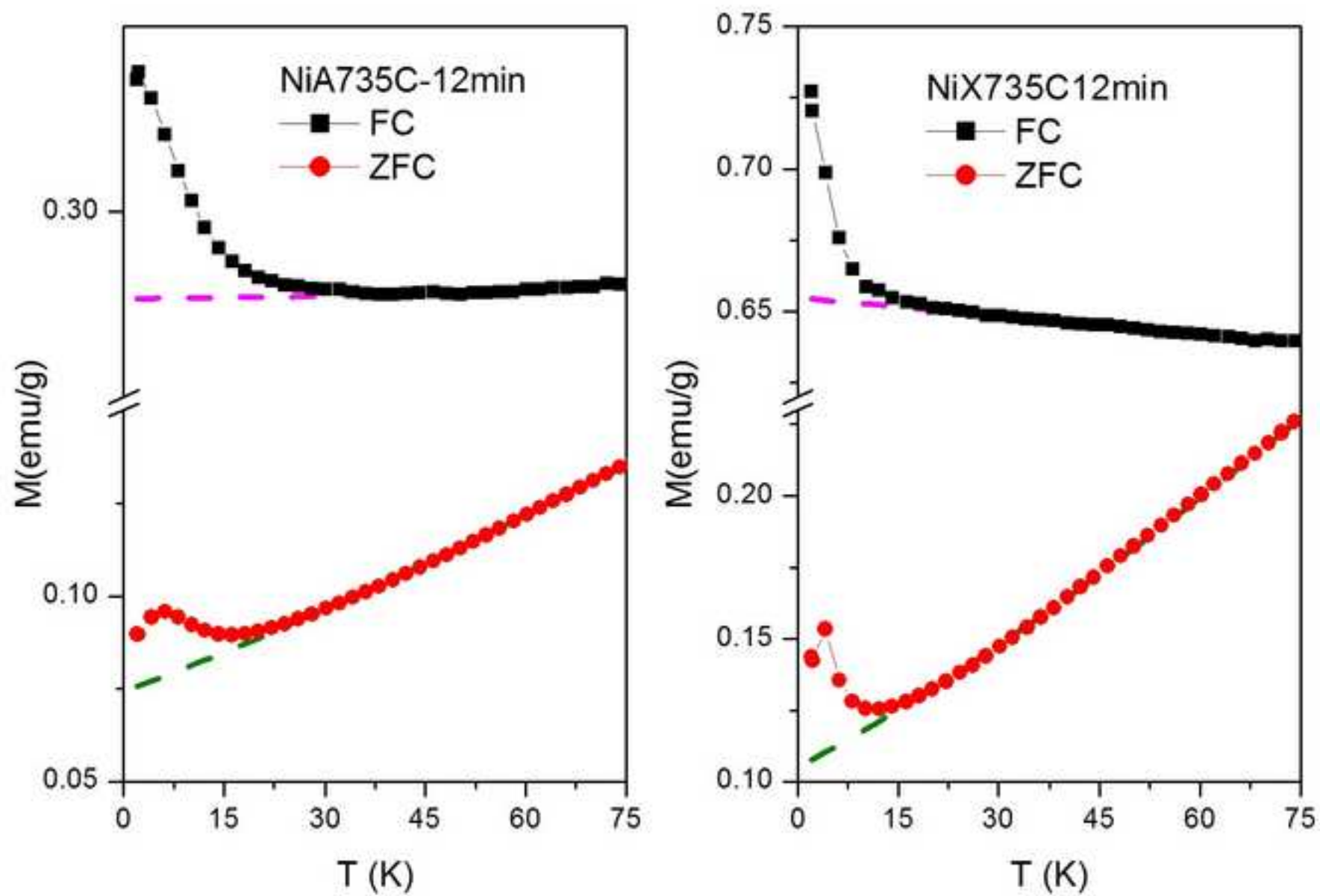


Figure 8  
[Click here to download high resolution image](#)

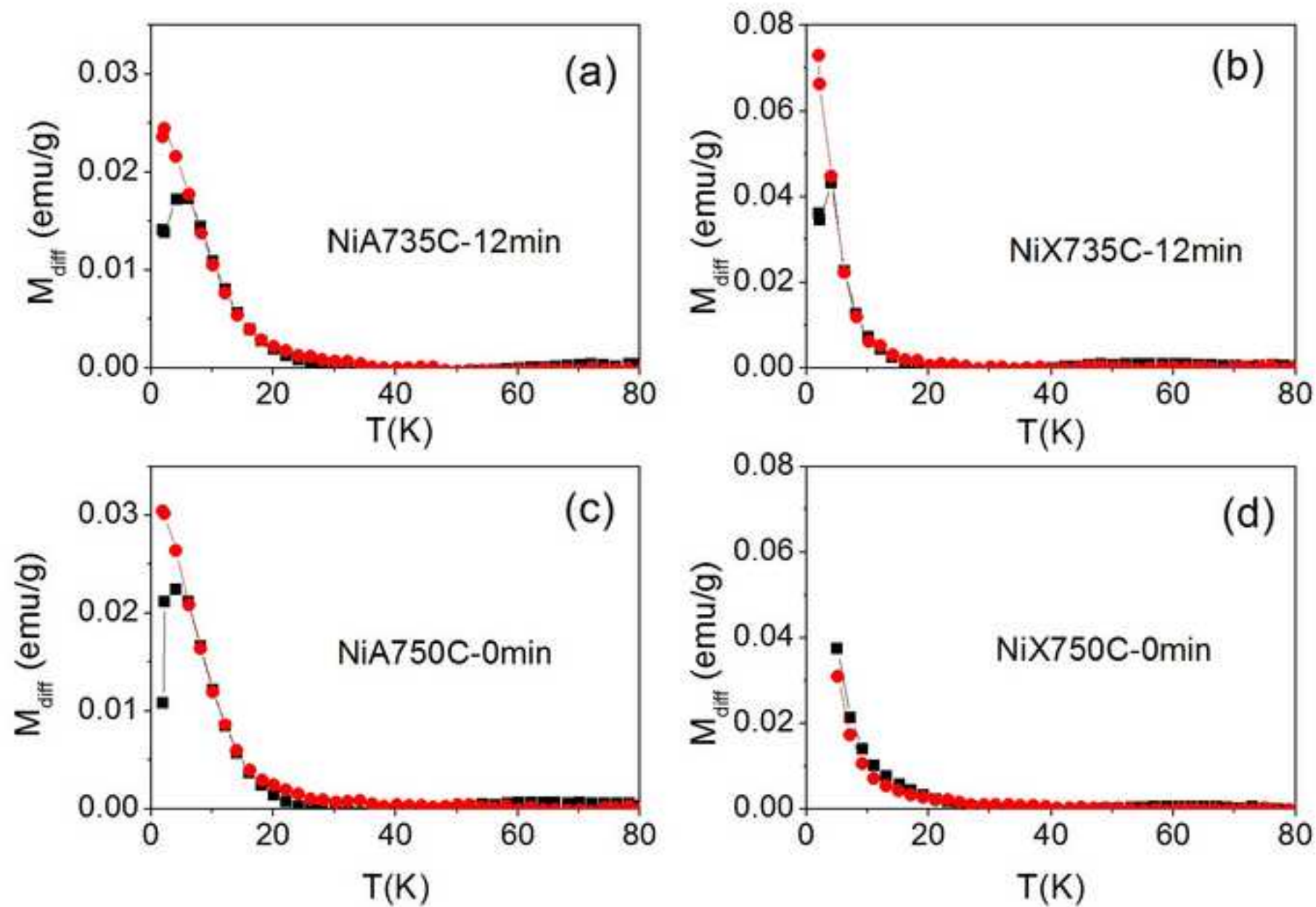


Figure 9  
[Click here to download high resolution image](#)

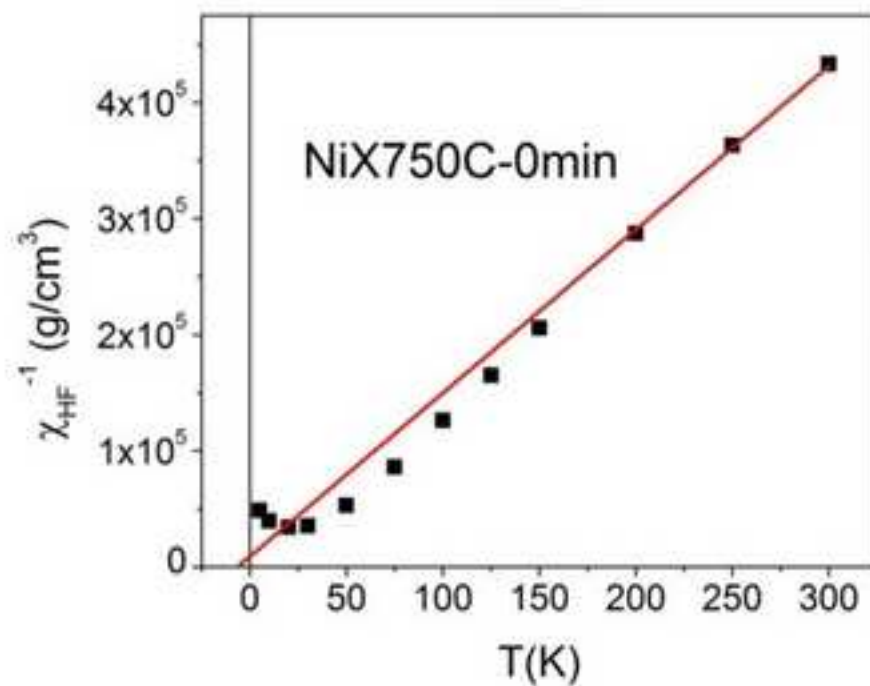
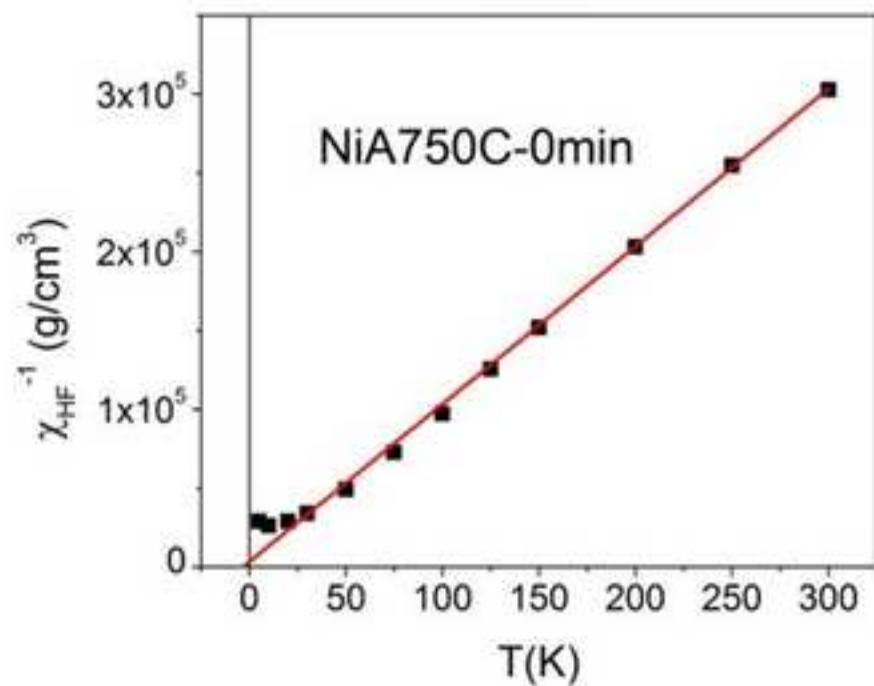
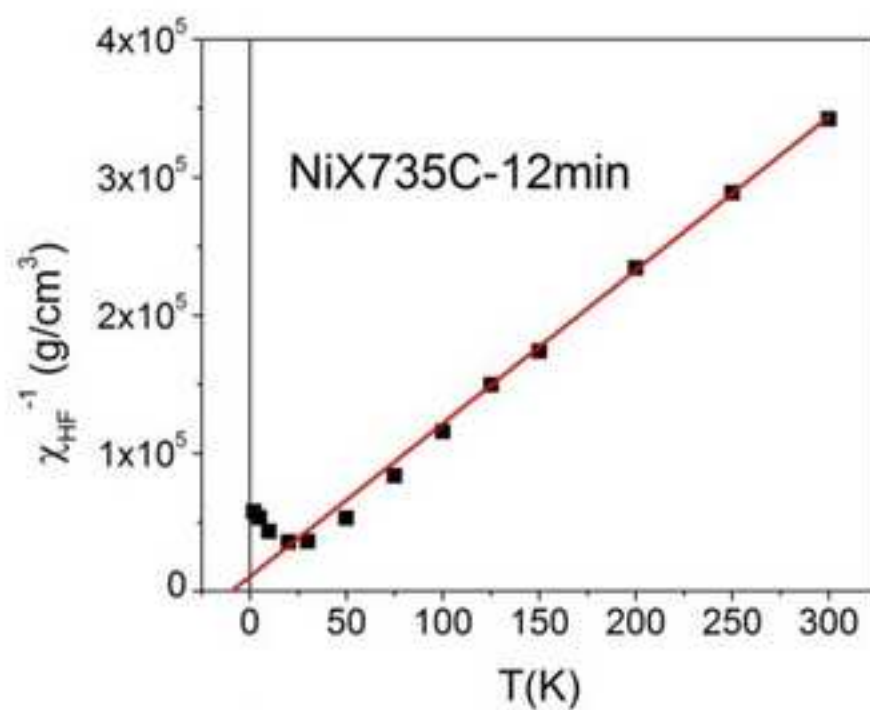
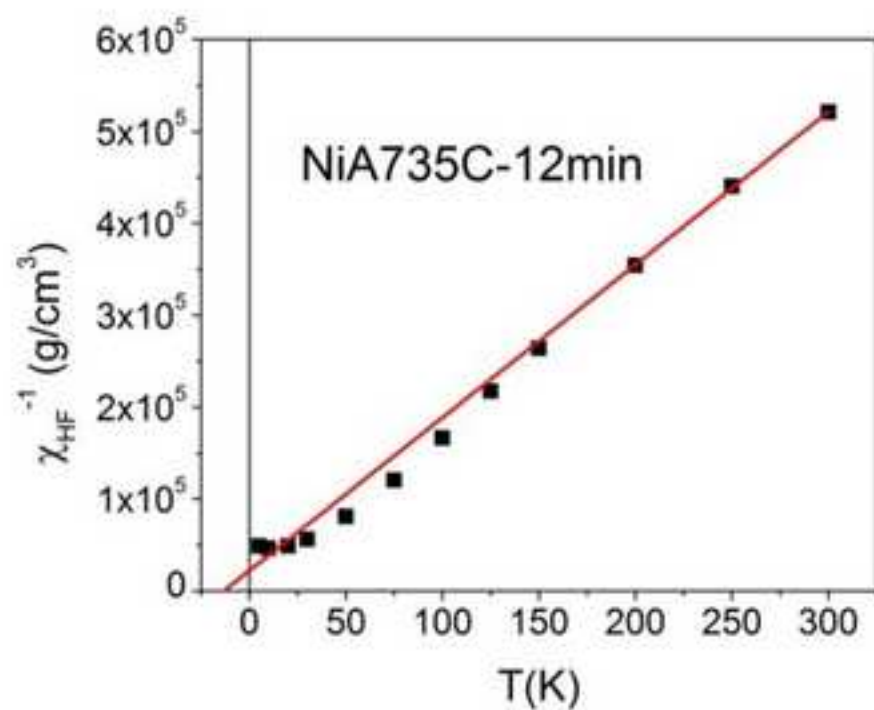




Figure 10  
[Click here to download high resolution image](#)

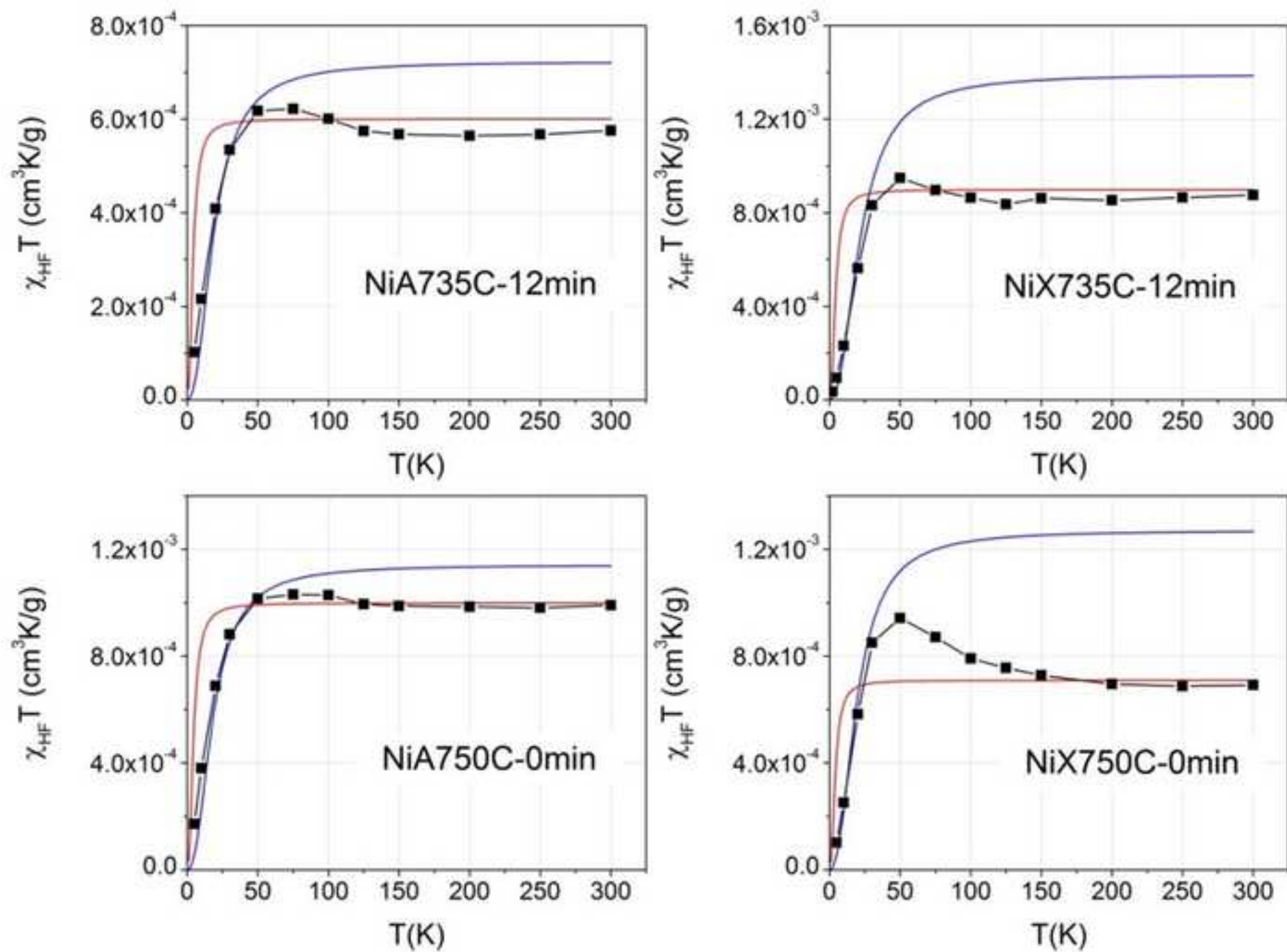


Figure 11  
[Click here to download high resolution image](#)

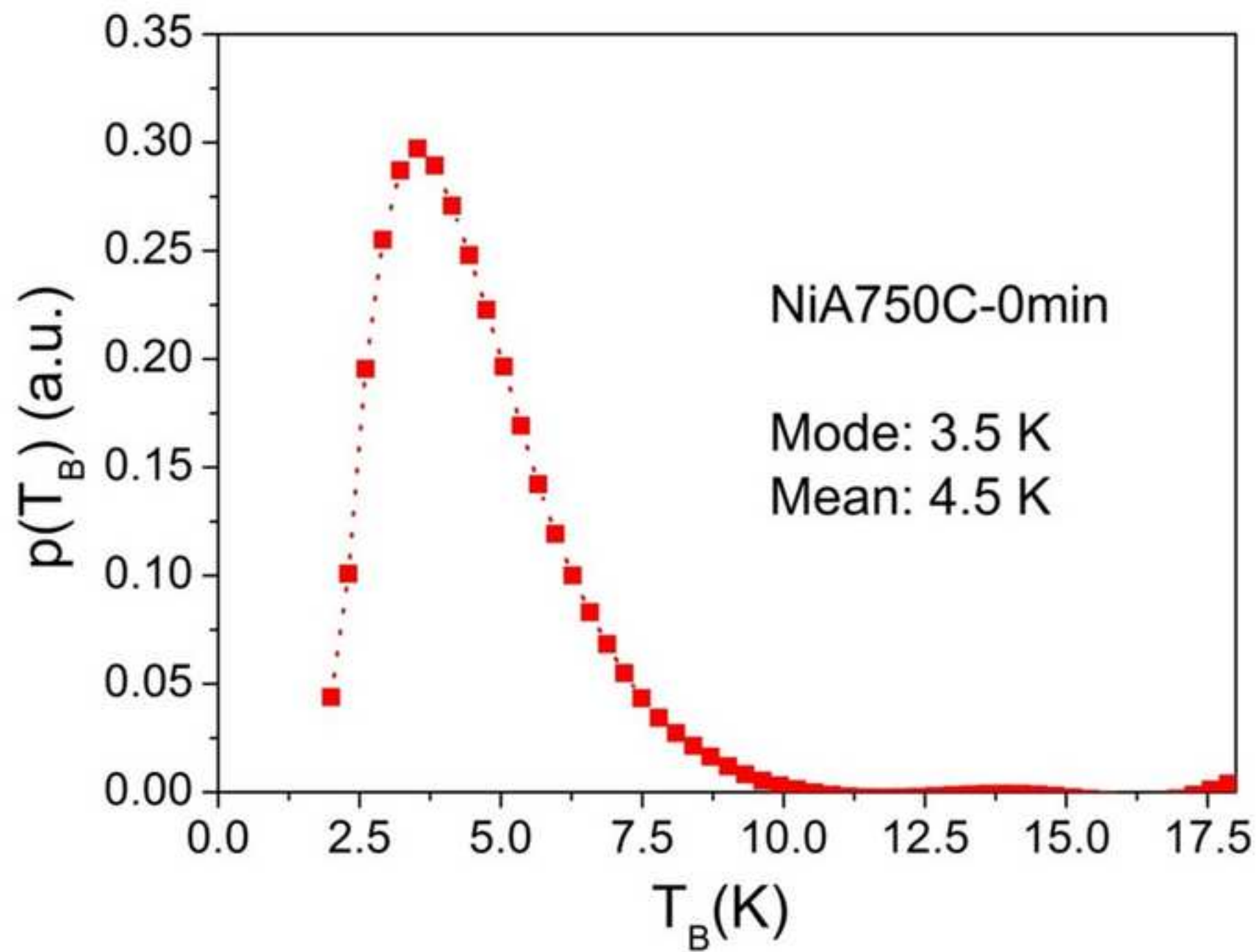




Figure 12  
[Click here to download high resolution image](#)

